Advances in Water Resources 208 (2026) 105215

Contents lists available at ScienceDirect

Advances in Water Resources

journal homepage: www.elsevier.com/locate/advwatres

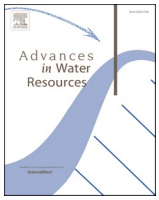

Chaotic advection in regional groundwater flow under periodic water table fluctuations: An analytical model with depth-dependent aquifer properties

Saurabh Maurya, Ratan Sarmah *, Ickkshaanshu Sonkar

Department of Civil Engineering, Indian Institute of Technology Ropar, India

ARTICLE INFO

Keywords:
Analytical solution
GITT
Depth-dependent hydraulic properties
Chaotic advection
Pathline
Pumping
Finite time Lyapunov exponent
Batchleor scale

ABSTRACT

Reliable prediction of groundwater flow dynamics is often hindered by the assumption of uniform aquifer parameters, leading to biased estimates of hydraulic head. Despite their well-established depth-dependence relationship, most analytical solutions remain restricted to homogeneous or single-layer aquifer systems. This study develops a two-dimensional transient analytical model for a multilayer regional aquifer driven by a fluctuating water table, explicitly incorporating depth-dependent hydraulic conductivity and specific storage while accounting for pumping. The analytical solution is derived using the Generalized Integral Transform Technique (GITT), ensuring implicit continuity of head and flux across layer interfaces without requiring iterative eigenvalue estimation, providing a rigorous framework to capture the complexities of stratified aquifers. Model verification is performed against a benchmark single-layer solution, and independent validation is carried out with COMSOL Multiphysics simulations, showing excellent agreement. Parameter influence and reliability are further assessed through global sensitivity analysis and uncertainty evaluation. A novel contribution of this work is the identification of chaotic flow behaviour within a three-layer Tóthian basin, analyzed using the Finite-Time Lyapunov Exponent (FTLE). Results show that chaotic dynamics are most pronounced near the upper boundary, where FTLE values are significantly higher than in deeper zones and further enhancement is observed under periodic injection. Moreover, specific storage is found to enhance the swirly motion of particle trajectories, increasing residence times near pseudo-stagnation zones. The proposed analytical framework bridges a critical gap in multilayer transient flow modeling, advances the theoretical understanding of stratified aquifer systems, and provides a robust benchmark for numerical and field-scale groundwater investigations.

1. Introduction

Groundwater models play a crucial role in water resource management, contaminant transport prediction, and sustainable decision-making. Their reliability depends on accurate parameterization, as errors in key parameters like hydraulic conductivity and specific storage can lead to serious misinterpretations (Li et al., 2024). Overestimating hydraulic conductivity may over-predict contaminant spread, while underestimation can delay cleanup efforts by falsely assuming slower contaminant migration. Similarly, inaccurate estimation of specific storage may distort assessments of aquifer sustainability, leading to overexploitation or overly conservative management strategist (Chowdhury et al., 2022).

Over the decades, mathematical modeling of groundwater flow has evolved considerably, advancing from simple conceptual representations to sophisticated models that account for real-world complexities such as spatially variable hydraulic properties, and time-dependent boundary conditions. The accuracy of such models depends critically on the representation of aquifer properties and boundary conditions. In natural settings, porosity, hydraulic conductivity, and specific storage generally decrease with depth due to increasing effective stress, matrix compaction, and reduced pore connectivity. Numerous field and laboratory studies have consistently documented this depth-dependent variability (Amthor et al., 1994; Budd, 2001; Jiang et al., 2010; Wang et al., 2009). The decline in porosity and hydraulic conductivity with depth has long been recognized (Rushton and Chan, 1976; Saar and Manga, 2004), while more recent quantitative formulations by Shestakov (2002) and Kuang et al. (2021) have refined the description of depth-dependent specific storage.

The conceptual foundation for regional groundwater flow was established by Tóth (1962), who introduced the concept of nested flow systems within homogeneous, isotropic basins. Building on Tóth's foundational studies (Tóth, 1962; Tóth, 1963), subsequent analytical

* Corresponding author.
E-mail address: ratan@iitrpr.ac.in (R. Sarmah).

https://doi.org/10.1016/j.advwatres.2026.105215
Received 3 November 2025; Received in revised form 18 December 2025; Accepted 9 January 2026
Available online 10 January 2026

Nomenclature

L	Length of the domain
B_1, B_2, B	Thickness of the first layer, Thickness of the first and second layer, and total thickness of the aquifer, respectively
H_L	Amplitude of the local undulation
H_R	Amplitude of the regional undulation
P	Seasonal variation period
Q_0	Pumping rate
K_{zB_0}, K_{zB_1}, K_{zB_2}	Vertical hydraulic conductivity at $z = 0$, $z = B_1$, and $z = B_2$, respectively
K_{xB_0}, K_{xB_1}, K_{xB_2}	Horizontal hydraulic conductivity at $z = 0$, $z = B_1$, and $z = B_2$, respectively
S_{sr1}, S_{sr2}, S_{sr3}	Residual specific storage for the top, middle, and bottom aquifer layer, respectively
S_{sB_0}, S_{sB_1}, S_{sB_2}	Specific storage at $z = 0$, $z = B_1$, and $z = B_2$, respectively
λ_1, λ_2, λ_3	Decay index for the top, middle, and bottom aquifer layer, respectively
A_1, A_2, A_3	Decay coefficient for the top, middle, and bottom aquifer layer, respectively
S_y	Specific yield
Ω_i	Domain of each layer of aquifer, $i = 1, 2, 3$
ε	Damping coefficient
f	Number of local topographic undulation
t_s	Pump starting time
t_d	Duration of the pump active phase
T_P	The time period between consecutive pulses
N_p	The total number of pulses
θ_0	The surface porosity
h_i^{st}	Steady state solution, $i = 1, 2, 3$
ω	Dimensionless response time
V_i	Filter function, satisfy the non-homogenous boundary conditions for each layer, $i = 1, 2, 3$
U	Transient solution, satisfy the homogenous boundary and inhomogeneous initial condition
C_{ki}, D_{ki}	Spatial coefficients of filter function, $k = 0,\ 1,\ 2\ldots\infty$ and $i = 1, 2, 3$
R_k	Temporal Coefficients of filter function, $k = 0,\ 1,\ 2\ldots\infty$ and $i = 1, 2, 3$
γ_{ki}	Vertical Eigenvalues, $k = 0,\ 1,\ 2\ldots\infty$ and $i = 1, 2, 3$
α_m, and β_n	Orthogonality conditions of the eigenfunctions along x and z direction, respectively, $m = 0,\ 1,\ 2\ldots\infty$ and $n = 1,\ 2,\ 3\ldots\ \infty$
T_{mn}	Transient coefficients, $m = 0,\ 1,\ 2\ldots\infty$ and $n = 1,\ 2,\ 3\ldots\ \infty$
$\mathbf{v}$	Darcy flux (v_x,v_z), along x and z direction, respectively
l_B	Batchelor scale
l_s	Characteristic length
s_0	Initial filament thickness
γ	Stretching rate
D_m	Molecular diffusion

studies examined steady-state flow structures (Jiang et al., 2011; J. Z. Wang et al., 2017; Wang et al., 2015; X. S. Wang et al., 2017; Zlotnik et al., 2015, 2011), while others have examined transient responses to periodically fluctuating water tables under constant hydraulic parameters (Das and Sarmah, 2025; Vandenberg, 1980; Zhao et al., 2018). Recognizing the stratified nature of aquifers, later studies extended these models to multilayered systems under steady-state conditions (Craig, 2008; Freeze and Witherspoon, 1966; Selim, 1975; Selim et al., 1975), offering more realistic representations of geological heterogeneity. To further enhance model realism, several investigations have incorporated depth-dependent hydraulic conductivity to reflect vertical variability (Das et al., 2026; Jiang et al., 2011; Wang et al., 2017; Wang et al., 2015; Zlotnik et al., 2011) under steady-flow assumptions. Recently, Zhang et al. (2025) developed a three-dimensional analytical model assuming uniform aquifer properties to analyze pseudo-stagnation points, providing new insights into groundwater flow behavior under simplified yet analytically tractable conditions.

While several studies have incorporated depth-dependent hydraulic conductivity under steady-flow conditions, most continue to treat hydrogeological parameters as constants under transient forcing. This simplification primarily stems from the mathematical challenges associated with deriving transient analytical solutions for layered aquifers, which require explicit enforcement of head and flux continuity at layer interfaces for all times. Solving such problems is inherently complex because conventional analytical techniques, such as the separation of variables method, demand iterative procedures to determine eigenvalues and coefficients for each layer (Aryeni and Ginting, 2022; Liu and Si, 2008; Sarmah et al., 2022). Alternatively, Laplace transform-based approaches demand solving partial differential equations in the Laplace domain and performing numerical inversion to recover temporal solutions. The analytical complexity increases rapidly with the number of layers and becomes even more formidable when aquifer properties vary spatially within individual layers, as in systems characterized by depth-dependent hydraulic properties. Consequently, transient analytical formulations incorporating both layering and depth-dependent hydraulic properties remain scarce.

Transient groundwater flow models developed for Tóthian basins under periodic top boundary forcing (Das and Sarmah, 2025; Zhang et al., 2025; Zhao et al., 2018) have primarily focused on particle pathlines and stagnation point dynamics to interpret subsurface flow behavior. Beyond Tóthian systems, periodic (tidal) boundary forcings have been employed in groundwater models to investigate the emergence of chaotic advection (Hazas et al., 2023; Tajima and Dentz, 2025; Trefry et al., 2019), a phenomenon first introduced by Aref (1984) to describe the intricate motion of fluid particles in laminar flows through repeated stretching and folding. In two-dimensional incompressible flow fields, the stream function serves as the Hamiltonian, rendering the system mathematically analogous to classical Hamiltonian dynamics. Under steady conditions, particle trajectories remain confined to streamlines, exhibiting regular motion; however, time-dependent forcing makes the system non-integrable, enabling the development of chaotic particle trajectories (Aref, 2002; Bagtzoglou and Oates, 2007).

The potential emergence of chaotic advection in natural groundwater systems is of growing interest, particularly due to its implications for solute transport and in situ remediation, where effective contaminant degradation depends on the mixing efficiency between treatment solutions and ambient groundwater. Since natural groundwater flow is predominantly laminar, inherent mixing is limited, constraining reaction rates. To overcome this, Sposito (2006) proposed engineered well configurations to enhance mixing under laminar conditions. Bagtzoglou and Oates (2007) demonstrated that oscillatory pumping from a three-well system can induce chaotic advection, significantly improving solute mixing and plume dispersion. Similarly, Trefry et al. (2012) showed that a rotating dipole well arrangement can generate time-dependent potential flow fields that promote efficient mixing, while laboratory experiments by Zhang et al. (2009) confirmed that oscillatory pumping enhances plume interface area and mixing efficiency in porous media.

Despite these advances, the possibility of naturally induced chaotic advection resulting from periodic water table oscillations coupled with

depth-dependent hydraulic properties remains largely unexplored in regional groundwater basins. Understanding such naturally driven mechanisms is critical for improving predictions of solute transport, reactive mixing, and residence time distributions, as well as for optimizing aquifer remediation, and geothermal recovery (Faybishenko, 2005; Lester et al., 2025).

Analytical solutions remain indispensable in hydrogeological research because they offer conceptual clarity, computational efficiency, and serve as critical benchmarks for validating numerical models. This study develops a two-dimensional transient analytical model for groundwater flow in a multilayer regional aquifer subjected to periodic boundary forcing and pumping, while incorporating depth-dependent hydraulic conductivity and specific storage. The formulation satisfies continuity across layer interfaces without iterative eigenvalue estimation. To the best of our knowledge, it provides the first analytical treatment that combines multilayer stratification, depth-varying properties, and pumping under transient regional conditions. By unifying these elements, the model addresses a longstanding gap in analytical hydrogeology and provides a robust benchmark for transient flow simulations in heterogeneous aquifers.

A key contribution of this work is the identification of chaotic flow behavior in a layered regional groundwater system, a phenomenon not previously reported. This result offers new insights into the dynamic responses of stratified aquifers under transient stresses.

The remainder of the paper is organized as follows: Section 2 presents the model formulation and derivation of the analytical solution, Section 3 discusses the results and their broader implications, with future perspectives and Section 4 concludes with key findings.

2. Conceptual and mathematical formulation

2.1. Conceptual framework and physical domain

The present study advances the classical concept of nested groundwater flow systems in topographically driven basins, originally formulated by Tóth (1963), by introducing a heterogeneous, layered aquifer subjected to an unsteady water-table boundary. The heterogeneity arises from depth-dependent variations in porosity caused by mechanical compaction of sediments under increasing lithostatic stress (Jiang et al., 2010) which induces systematic declines in both hydraulic conductivity and specific storage due to their porosity dependence.

The flow domain extends horizontally from a regional topographic valley to an opposing summit, separated by a distance L. Owing to topographic symmetry, both the valley and summit act as no-flow divides. The water table generally follows the land-surface profile but coincides with it at the valley bottoms, representing perennial stream channels that anchor the phreatic surface. Vertically, the domain extends from the transient water table to an underlying impermeable bedrock located at depth B, measured from the minimum water-table elevation. Since the undulating water-table surface introduces geometric irregularity that complicates analytical derivations, a simplifying assumption is adopted following Zlotnik et al. (2015): the amplitude of the water-table undulation is small compared to the total aquifer thickness. Under this assumption, the flow region can be idealized as a rectangular computational domain, obtained by neglecting the shallow portion above the leftmost valley point.

Accordingly, the two-dimensional rectangular cross-section shown by the dashed outline in Fig. 1 defines the computational domain. The coordinate origin is located at the left valley, with the x-axis extending horizontally to the right and the z-axis directed vertically downward. The regional aquifer is conceptualized as a three-layered system, each layer characterized by distinct hydrogeological properties and intra-layer heterogeneity represented by depth-dependent variations in $K_x(z)$,$K_z(z)$, and $S_s(z)$. The layers are denoted as I, II, and III, arranged from top to bottom, defined by the region:

$$\Omega_1 = \{(x,z)|0<x<L,\ 0<z<B_1\},\ \Omega_2 = \{(x,z)|0<x<L,\ B_1<z<B_2\},\ \Omega_3 = \{(x,z)|0<x<L,\ B_2<z<B\},$$

where B_1 and B_2 represents depth to the layer interfaces [L], measured from the top surface of the flow domain. Hence, the entire flow domain is expressed as $\Omega = \bigcup_{i=1}^{3}\Omega_i$.

Aquifer systems and hydrogeologic basins are typically composed of layered sediments or rocks, where small variations in material properties such as grain size or clay content can produce orders-of-magnitude differences in permeability (Gassiat et al., 2013). In the present model, the second layer represents a low-conductivity layer with hydrogeological properties distinct from the upper and lower layers, reflecting a common structural feature in multilayer groundwater systems. Similar aquifer-aquitard–aquifer arrangements have been used in several studies (Cihan et al., 2022; Feng et al., 2021; Sedghi et al., 2018; Souvik et al., 2020).

2.2. Topography and water-table configuration

The land-surface topography is represented as a periodically varying profile, characterized by alternating depressions and summits occurring at regular intervals (Zhao et al., 2018):

$$Z_{LS}(x) = H_R\left[1-\cos\left(\pi\frac{x}{L}\right)\right] + H_L\left[1-\cos\left(f\pi\frac{x}{L}\right)\right], \tag{1}$$

where H_R and H_L are the regional and local topographic amplitudes [L], respectively, and $f>3$ is an odd integer ensuring that the right boundary corresponds to the maximum elevation (Jiang et al., 2011). Since the water table typically mirrors the land surface but with reduced amplitude, its spatial variation is expressed by applying a damping coefficient $\varepsilon(0<\varepsilon<1)$. In this study, $\varepsilon = 0.85$ is adopted, while in field applications it is a fitted parameter obtained from observed water-level data. Seasonal fluctuations are superimposed on the spatially damped water-table surface following Zhao et al. (2018) giving:

$$h_{WT}(x,t) = H_R\left[1-\cos\left(\pi\frac{x}{L}\right)\right] + \varepsilon H_L\left[1-\cos\left(f\pi\frac{x}{L}\right)\right]\sin^2\left(\pi\frac{t}{P}\right), \tag{2}$$

where $P = 365$ days represents the annual period of water-table oscillation [T].

2.3. Governing equation

Let the position vector be $\mathbf{r} = (x, z)$, and the pumping-well location be $\mathbf{r}_0 = (x_0, z_0)$. Transient saturated flow within a heterogeneous, layered aquifer system is governed by the continuity equation and Darcy's law, which, in compact tensor form, can be expressed as:

$$S_{si}(z)\frac{\partial h_i(\mathbf{r},t)}{\partial t} = \nabla.[\mathbf{K}_i(z)\nabla h_i(\mathbf{r},t)] - \delta_i^j Q(t)\delta(\mathbf{r}-\mathbf{r}_0),\ \mathbf{r}\in\Omega_i,\ i \in \{1,\ 2,\ 3\}. \tag{3}$$

Here, $h_i(\mathbf{r}, t)$ denotes the hydraulic head in layer i; $S_{si}(z)$ is the depth-dependent specific storage in the i^{th} layer; $\nabla = \begin{bmatrix}\frac{\partial}{\partial x}\\ \frac{\partial}{\partial z}\end{bmatrix}$ is the nabla operator, and $\mathbf{K}_i(z) = \begin{bmatrix}K_{xi}(z) & 0\\ 0 & K_{zi}(z)\end{bmatrix}$ is the anisotropic hydraulic conductivity tensor. The Dirac delta function $\delta(\mathbf{r}-\mathbf{r}_0)$ localizes the pumping influence in the spatial domain (Suk et al., 2022), while the Kronecker delta δ_i^j ensures that the sink term is active only within the layer containing the well ($i=j$) and vanishes elsewhere.

The temporal pumping schedule is defined as:

$$Q(t) = Q_0 \sum_{p=0}^{N_p-1} \{H[t-(t_s+pT_p)] - H[t-(t_s+pT_p+t_d)]\}, \quad (4)$$

where $Q_0$is the constant pumping rate magnitude [L^2/T] and $H(\cdot)$ is the heavy side step function, t_s represents the pump starting time [T], t_d is the duration of the pump active phase [T], T_P is the time period between consecutive pulses [T], and N_p is the total number of pulses applied.

The initial and boundary conditions, consistent with the schematic shown in Fig. 1, are given by:

Initial condition

$$h_i(x,\ z,\ 0) = h_i^{st}(x,\ z), \quad (5)$$

where $h_i^{st}(x,\ z)$ represents the initial condition of the flow problem. It corresponds to the steady-state solution of Eq. (3), obtained under a regional water table imposed at the upper boundary, neglecting transient surface undulations and pumping stresses.

No-flow boundary conditions are imposed along the lateral and bottom boundaries:

$$\frac{\partial h_i(0,\ z,\ t)}{\partial x} = 0, \quad (6)$$

$$\frac{\partial h_i(L,\ z,\ t)}{\partial x} = 0, \quad (7)$$

$$\frac{\partial h_3(x,\ B,\ t)}{\partial z} = 0. \quad (8)$$

The head and flow continuity conditions at the interfaces between layers are given by:

$$h_i(x,\ B_i^-,\ t) = h_{i+1}(x,\ B_i^+,\ t), \quad (9)$$

$$K_{zi}(B_i^-)\frac{\partial h_i(x,\ B_i^-,\ t)}{\partial z} = K_{z(i+1)}(B_i^+)\frac{\partial h_{i+1}(x,\ B_i^+,\ t)}{\partial z}. \quad (10)$$

A Dirichlet boundary condition is applied at the top boundary to represent the water table variation:

$$h_1(x,\ 0,\ t) = h_{WT}(x,\ t). \quad (11)$$

With increasing depth, aquifer properties such as porosity, hydraulic conductivity, and specific storage generally decline due to enhanced effective stress from overburden pressure. These trends have been widely reported in field and theoretical studies (Amthor et al., 1994; Jiang et al., 2010; Saar and Manga, 2004; Wang et al., 2009). Following the semi-empirical model based on Athy's law, the porosity variation with depth is represented as (Jiang et al., 2010):

$$\theta(z) = \theta_0 \exp\left(-\frac{Az}{n}\right), \quad (12)$$

where θ_0 is the surface porosity [-], A is the decay coefficient [L^{-1}], and n is the permeability–porosity power-law exponent, typically ranging from 3 to 5. Here, $n = 4$ is adopted for pathline and travel-time analyses.

The corresponding depth-dependent hydraulic conductivities within the i^{th} layer are expressed as (Jiang et al., 2010; Jiang et al., 2009):

$$K_{xi}(z) = K_{xB_{i-1}^+} \exp[-A_i(z-B_{i-1})], \quad (13)$$

$$K_{zi}(z) = K_{zB_{i-1}^+} \exp[-A_i(z-B_{i-1})], \quad (14)$$

where $K_{xB_{i-1}^+}$ and $K_{zB_{i-1}^+}$ are the horizontal and vertical conductivities at the top surface of the i^{th} layer, respectively, $A_i$is layer-specific decay coefficient, and B_{i-1} is the depth to the i^{th} layer top measured from the top boundary (with $B_0 = 0$ for the upper most layer).

Field data also indicate a systematic decrease in specific storage with depth (Kuang et al., 2021; Shestakov, 2002). Following Kuang et al., (2021), this relationship is represented as:

$$\log(S_s) = \log(S_{Sr}) + [\log(S_{S0}) - \log(S_{Sr})]\left[\left(1+\frac{z}{1000}\right)^{-\lambda}\right]. \quad (15)$$

where S_{s0} represents the specific storage at the top of the aquifer, which corresponds to the maximum storage capacity due to low effective stress and larger pore spaces [L^{-1}]. The parameter S_{sr} denotes the minimum or residual specific storage attainable at great depth [L^{-1}], where increasing confining stress causes pore compression and reduced matrix compressibility (Kuang et al., 2021), and λ is an empirical fitting coefficient [-].

Expressed directly in terms of S_S for a layered system, becomes:

$$S_{si}(z) = S_{sri}\left[\frac{S_{SB_{i-1}^+}}{S_{sri}}\right]^{\left(1+\frac{z-B_{i-1}}{1000}\right)^{-\lambda_i}}, \quad (16)$$

where $S_{SB_{i-1}^+}$ is the specific storage at the top surface of the i^{th} layer, S_{Sri} is the residual specific storage for the i^{th} layer, and λ_i is an empirical fitting coefficient for the i^{th} layer.

The depth-dependent variations of the hydraulic parameters, along with the temporal pumping schedule considered in this study, are illustrated in Fig. 2, and the corresponding parameter values are summarized in Table 1 and Table C1.

2.4. Dimensionless transformation

To facilitate analytical development, the governing equations are expressed in dimensionless form as:

$$\begin{aligned}
h_{Di} &= \frac{h_i}{H_R},\\
x_D &= \frac{x}{L},\\
z_D &= \frac{z}{L},\\
t_D &= \frac{K_{z0}}{S_{sr1}L^2}t,\\
A_{Di} &= A_i L,\\
B_D &= \frac{B}{L},\\
B_{Di} &= \frac{B_i}{L},\\
Q_D &= \frac{Q}{K_{z0}H_R},\\
S_{sDi}(z_D) &= \left(\frac{S_{sri}}{S_{sr1}}\right)\left\{\frac{S_{SB_{i-1}^+}}{S_{sri}}\right\}^{\left[1+\frac{L(z_D-B_{D(i-1)})}{1000}\right]^{-\lambda_i}},\\
K_{xDi}(z_D) &= \left(\frac{K_{xB_{i-1}^+}}{K_{z0}}\right)\exp[-A_{Di}(z_D-B_{D(i-1)})],\\
K_{zDi}(z_D) &= \left(\frac{K_{zB_{i-1}^+}}{K_{z0}}\right)\exp[-A_{Di}(z_D-B_{D(i-1)})],\\
\omega &= \frac{S_{sr1}\pi L^2}{K_{z0}P}.
\end{aligned} \quad (17)$$

The parameter ω in Eq. (17) is a dimensionless measure of the aquifer's response time, comparing the diffusive response time $\frac{S_{sr1}L^2}{K_{z0}}$ with the period P of the imposed water-table fluctuations. The ratio $\frac{\omega}{\pi}$ characterizes the ability of the upper aquifer layer to follow and transmit the

periodic water-table variations (Vandenberg, 1980; Zhao et al., 2018).

Substituting these dimensionless variables into the governing flow equation [Eq. (3)], along with the initial and boundary conditions [Eqs. (5)-(11)], gives the following non-dimensional form:

$$S_{sDi}(z_D)\frac{\partial h_{Di}(\mathbf{r}_D,\,t_D)}{\partial t_D}=\nabla_D.[\mathbf{K}_{Di}(z_D)\nabla_D h_{Di}(\mathbf{r}_D,\,t_D)]-\delta_i^j Q_D(t_D)\delta(\mathbf{r}_D-\mathbf{r}_{D0}),\ \mathbf{r}_D\in\Omega_{Di}, \tag{18}$$

where $\nabla_D=\begin{bmatrix}\frac{\partial}{\partial x_D}\\ \frac{\partial}{\partial z_D}\end{bmatrix}$ and $\mathbf{K}_{Di}(z_D)=\mathrm{diag}[K_{xDi}(z_D),K_{zDi}(z_D)]$.with the corresponding initial and boundary conditions:

$$h_{Di}(x_D,\ z_D,\ 0)=h_{Di}^{st}(x_D,\ z_D), \tag{19}$$

$$\frac{\partial h_{Di}(0,\ z_D,\ t_D)}{\partial x_D}=0, \tag{20}$$

$$\frac{\partial h_{Di}(1,\ z_D,\ t_D)}{\partial x_D}=0, \tag{21}$$

$$\frac{\partial h_{D3}(x_D,\ B_D,\ t_D)}{\partial z_D}=0, \tag{22}$$

$$h_{Di}\left(x_D,\ B_{Di}^{-},\ t_D\right)=h_{D(i+1)}\left(x_D,\ B_{Di}^{+},\ t_D\right), \tag{23}$$

$$K_{zDi}\left(B_{Di}^{-}\right)\frac{\partial h_{Di}\left(x_D,\ B_{Di}^{-},\ t_D\right)}{\partial z_D}=K_{zD(i+1)}\left(B_{Di}^{+}\right)\frac{\partial h_{D(i+1)}\left(x_D,\ B_{Di}^{+},\ t_D\right)}{\partial z_D} \tag{24}$$

In Eq. (19), $h_{Di}^{st}(x_D,\ z_D)$ represents the dimensionless initial condition of the flow problem. The explicit form of h_{Di}^{st} is presented in the following section, where the analytical solution of the flow problem is developed.

2.5. Solution for hydraulic head

The transient flow within the stratified basin, subjected to water-table fluctuations and depth-dependent aquifer properties, is analyzed using the Generalized Integral Transform Technique (GITT), which requires homogeneous boundary conditions (Deng et al., 2014; Liu et al., 2000). Since the top boundary condition [Eq. (25)] is non-homogeneous, the dimensionless hydraulic head is decomposed as:

$$h_{D1}(x_D,\,0,\,t_D)=h_{DWT}(x_D,\,t_D)=[1-\cos(\pi x_D)]+\varepsilon\left(\frac{H_L}{H_R}\right)[1-\cos(f\pi x_D)]\sin^2(\omega t_D). \tag{25}$$

$$h_{Di}(\mathbf{r}_D,\ t_D)=U(\mathbf{r}_D,\ t_D)+V_i(\mathbf{r}_D,\ t_D), \tag{26}$$

where V_i satisfies the non-homogeneous Dirichlet condition at the top and no-flow elsewhere. In one-dimensional cases, V_i can be expressed as a simple linear function meeting both end conditions (Deng et al., 2014). However, for two-dimensional domains, constructing such a function that meets all boundary constraints is non-trivial and requires a more systematic approach. Once V_i is defined, the residual component $U=h_{Di}-V_i$ inherently satisfies homogeneous boundary conditions and thus serves as the transformed variable in the GITT framework. Here, V_i acts as a filtering function that extracts the non-homogeneous influence of the upper boundary, ensuring a homogeneous formulation for U.

In this study, V_i is defined as the steady-state solution of the governing equation (with $S_{sD}=0$), subject to the prescribed transient upper boundary while neglecting pumping effects. This choice preserves the mathematical consistency of the formulation while simplifying its construction. The remaining component U is subsequently solved through the GITT procedure.

The governing equation for V_i in the dimensionless form is given by:

$$\nabla_D.[\mathbf{K}_{Di}(z_D)\nabla_D V_i(\mathbf{r}_D,\ t_D)]=0,\ \mathbf{r}_D\in\Omega_{Di}, \tag{27}$$

subjected to the boundary conditions:

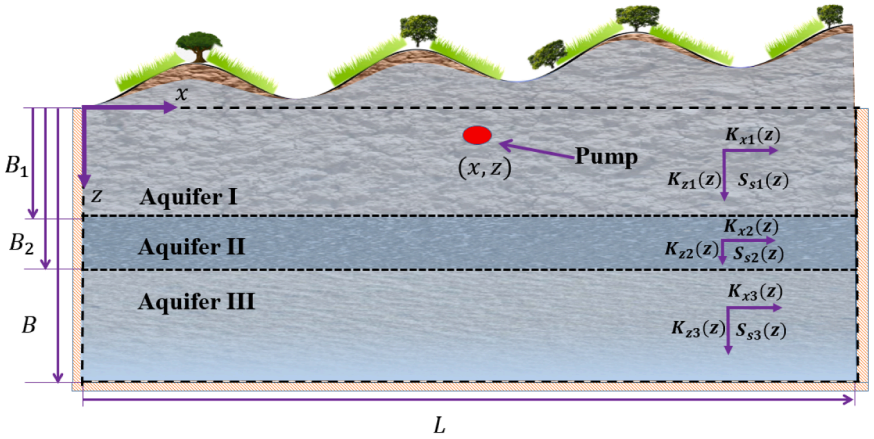

Fig. 1. Two-dimensional representation of three-layered regional groundwater flow basin.

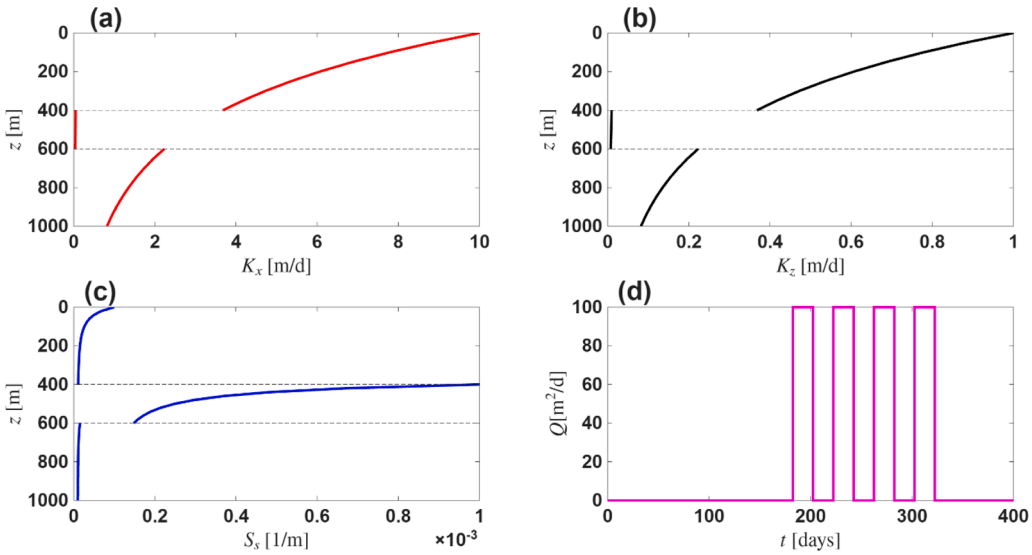

Fig. 2. Layer-wise spatial variation of (a) horizontal hydraulic conductivity, (b) vertical hydraulic conductivity, (c) specific storage, and (d) temporal pumping schedule considered in the present study.

$$\frac{\partial V_i(0,\ z_D,\ t)}{\partial x_D} = 0, \tag{28}$$

$$\frac{\partial V_i(1,\ z_D,\ t_D)}{\partial x_D} = 0, \tag{29}$$

$$\frac{\partial V_3(x_D,\ B_D,\ t_D)}{\partial z_D} = 0, \tag{30}$$

$$V_i\left(x_D,\ B_{Di}^{-},\ t_D\right) = V_{i+1}\left(x_D,\ B_{Di}^{+},\ t_D\right), \tag{31}$$

$$K_{zDi}\left(B_{Di}^{-}\right)\frac{\partial V_i\left(x_D,\ B_{Di}^{-},\ t_D\right)}{\partial z_D} = K_{zD(i+1)}\left(B_{Di}^{+}\right)\frac{\partial V_{i+1}\left(x_D,\ B_{Di}^{+},\ t_D\right)}{\partial z_D}, \tag{32}$$

$$V_1(x_D,\ 0,\ t_D) = h_{DWT}(x_D,\ t_D) = [1-\cos(\pi x_D)] + \varepsilon\left(\frac{H_L}{H_R}\right)[1-\cos(f\pi x_D)]\sin^2(\omega t_D). \tag{33}$$

The analytical representation of V_i is obtained by solving Eq. (27) subject to Eqs. (28)-(33). Closed-form solutions are derived for individual layers and then coupled through continuity of head and flux across interfaces. The explicit solution is expressed as:

$$V_i(\boldsymbol{r}_D,\ t_D) = \exp\left(\frac{A_{Di}}{2}z_D\right)\sum_{k=0}^{\infty} R_k(t_D)\cos(k\pi x_D)[C_{ki}\cosh(\gamma_{ki}z_D) + D_{ki}\sinh(\gamma_{ki}z_D)], \tag{34}$$

where $R_k(t_D)$ are the temporal coefficients, γ_{ki} are vertical eigenvalues, and C_{ki} and D_{ki} are constants determined from boundary conditions (details in Appendix A).

It is noteworthy that the initial condition for the flow problem, $h_{Di}^{st}(\boldsymbol{r}_D)$, is obtained by setting $t_D = 0$ in the expression for V_i, since this function originates from the steady-state form of the governing equation under the imposed transient boundary condition. Substituting $t_D = 0$ into Eq. (34) provides the hydraulic head distribution corresponding to the water table configuration at the initial instant. Alternatively, $h_{Di}^{st}(\boldsymbol{r}_D)$ can be interpreted as the steady-state solution of the flow system under the regional water table, which coincides with the initial state of the upper boundary, as indicated by Eq. (25), when $t_D = 0$. Thus,

$$h_{Di}^{st}(\boldsymbol{r}_D) = V_i(\boldsymbol{r}_D,\ 0). \tag{35}$$

The subsequent step entails deriving the analytical expression for $U(\boldsymbol{r}_D,\ t_D)$ subject to homogeneous boundary conditions. This is achieved by reformulating the dimensionless governing equation [Eq. (18)] in terms of $U(\boldsymbol{r}_D,\ t_D)$ using Eq. (26), given by:

$$S_{sDi}(z_D)\left(\frac{\partial U}{\partial t_D} + \frac{\partial V_i}{\partial t_D}\right) = \nabla_D.[\mathbf{K}_{Di}(z_D)\nabla_D U] - \delta_i^j Q_D(t_D)\delta(\mathbf{r}_D - \mathbf{r}_{D0}),\ \ \mathbf{r}_D \in \Omega_{Di}, \tag{36}$$

subjected to

$$U(x_D,\ z_D,\ 0) = h_{Di}^{st}(x_D,\ z_D) - V_i(x_D,\ z_D,\ 0) = 0, \tag{37}$$

$$\frac{\partial U(0,\ z_D,\ t_D)}{\partial x_D} = 0, \tag{38}$$

Table 1
Model parameter values used in the analysis.

1	Length of the domain (L)	10,000 m
2	Thickness of the aquifer (B)	1,000 m
3	Thickness of the first layer of the soil (B_1)	400 m
4	Thickness of the second layer of the soil ($B_2 - B_1$)	200 m
5	Thickness of the second layer of the soil ($B - B_2$)	400 m
6	Amplitude of the local undulation (H_L)	50 m
7	Amplitude of the regional undulation (H_R)	50 m
8	Seasonal variation period (P)	365 days
9	Pumping rate (Q_0)	100 m^2/d

$$\frac{\partial U(1,\ z_D,\ t_D)}{\partial x_D} = 0, \tag{39}$$

$$\frac{\partial U(x_D,\ B_D,\ t_D)}{\partial z_D} = 0, \tag{40}$$

$$U\left(x_D,\ B_{Di}^{-},\ t_D\right) = U\left(x_D,\ B_{Di}^{+},\ t_D\right), \tag{41}$$

$$K_{zDi}\left(B_{Di}^{-}\right)\frac{\partial U\left(x_D,\ B_{Di}^{-},\ t_D\right)}{\partial z_D} = K_{zD(i+1)}\left(B_{Di}^{+}\right)\frac{\partial U\left(x_D,\ B_{Di}^{+},\ t_D\right)}{\partial z_D}, \tag{42}$$

$$U(x_D,\ 0,\ t_D) = 0. \tag{43}$$

While, V_i is derived layer-wise, solving Eq. (36) for U separately in each layer is mathematically cumbersome due to interfacial coupling through time-dependent terms. Prior studies indicate that this typically requires iterative determination of eigenvalues and coefficients (Aryeni and Ginting, 2022; Liu and Si, 2008; Sarmah et al., 2022). To overcome this, a unified domain-wide formulation is adopted (Deng et al., 2014; Bashist et al., 2026), where the layer-wise parameters (S_{sDi},K_{xDi} and K_{zDi}) are defined as piecewise continuous functions in the form:

$$S_{sD}(z_D) = \begin{cases} S_{sD1}, & \mathbf{r}_D \in \Omega_{D1}, \\ S_{sD2}, & \mathbf{r}_D \in \Omega_{D2}, \\ S_{sD3}, & \mathbf{r}_D \in \Omega_{D3} \end{cases} \tag{44}$$

$$K_{xD}(z_D) = \begin{cases} K_{xD1}, & \mathbf{r}_D \in \Omega_{D1}, \\ K_{xD2}, & \mathbf{r}_D \in \Omega_{D2}, \\ K_{xD3} & \mathbf{r}_D \in \Omega_{D3}, \end{cases} \tag{45}$$

and

$$K_{zD}(z_D) = \begin{cases} K_{zD1}, & \mathbf{r}_D \in \Omega_{D1}, \\ K_{zD2}, & \mathbf{r}_D \in \Omega_{D2}, \\ K_{zD3} & \mathbf{r}_D \in \Omega_{D3}. \end{cases} \tag{46}$$

Using these definitions, Eq. (36) is reformulated for the full domain as:

$$S_{sD}(z_D)\left(\frac{\partial U}{\partial t_D} + \frac{\partial V}{\partial t_D}\right) = \nabla_D.[\mathbf{K}_D(z_D)\nabla_D U] - Q_D(t_D)\delta(\mathbf{r}_D - \mathbf{r}_{D0}),\ \mathbf{r}_D \in \Omega_D, \tag{47}$$

subject to the initial and boundary conditions defined in Eqs. (37)-(40) and (43), where $V = \begin{cases} V_1, & \mathbf{r}_D \in \Omega_{D1} \\ V_2, & \mathbf{r}_D \in \Omega_{D2} \\ V_3 & \mathbf{r}_D \in \Omega_{D3} \end{cases}$.

It is noted that Eq. (47) reproduces Eq. (36) within each layer through the definitions in Eqs. (44)-(46). Since the spatio-temporal variation of U is identical in both formulations, the interface condition given in Eq. (41) is inherently satisfied.

The corresponding dimensionless vertical flux is expressed as:

$$J_{z_D}(\mathbf{r}_D, t_D) = -K_{zD}(z_D)\frac{\partial U}{\partial z_D}. \tag{48}$$

When the pumping location lies within a layer and not at the interface, the dimensionless vertical flux across the interface can be written as:

$$J_{z_D}\left(x_D,\ B_{Di}^{-},\ t_D\right) = J_{z_D}\left(x_D,\ B_{Di}^{+},\ t_D\right). \tag{49}$$

Substituting Eq. (48) into Eq. (49) and incorporating Eq. (46) demonstrates that Eq. (49) is equivalent to Eq. (42). This confirms that the interfacial conditions [Eqs. (41) and (42)] are implicitly satisfied within Eq. (47). Therefore, while solving Eq. (47), there is no need to explicitly impose interface conditions, which provides a distinct advantage of this approach over existing methods.

The analytical expression for $U(\mathbf{r}_D, t_D)$ is obtained by solving Eq. (47) using the GITT (Deng et al., 2014; Mikhailov and Ozisik, 1983). Employing the orthogonality property of eigenfunctions, the solution for $U(\mathbf{r}_D, t_D)$ is expressed as:

$$U(x_D,\ z_D,\ t_D) = \sum_{m=0}^{\infty}\sum_{n=1}^{\infty} T_{mn}(t_D)\frac{\cos(m\pi x_D)}{(\alpha_m)^{\frac{1}{2}}}\frac{\sin\left[\frac{(1-2n)\pi}{2B_D}z_D\right]}{(\beta_n)^{\frac{1}{2}}}, \tag{50}$$

where α_m and β_n arise from the orthogonality conditions of the eigenfunctions in the horizontal and vertical directions, respectively, ensuring the proper normalization of the basis functions. These are defined as:

$$\alpha_m = \int_0^1 \cos^2(m\pi x_D)dx_D, \tag{51}$$

$$\beta_n = \int_0^{B_D} \sin^2\left[\frac{(1-2n)\pi}{2B_D}z_D\right]dz_D. \tag{52}$$

To determine the transient coefficients $T_{mn}(t_D)$, the integral operator $\int_0^1\int_0^{B_D}(\cdot)\frac{\cos(m\pi x_D)}{(\alpha_m)^{1/2}}\frac{\sin\left[\frac{(1-2n)\pi}{2B_D}z_D\right]}{(\beta_n)^{1/2}}dx_D dz_D$ is applied to Eq. (47), resulting in a system of ODEs for $T_{mn}(t_D)$:

$$\mathbf{E}\frac{d\mathbf{T}}{dt_D} + \mathbf{F}\mathbf{T}(t_D) = \mathbf{G}(t_D), \tag{53}$$

where the matrices for **E, F** and the vector $\mathbf{G}(t_D)$ are defined in Eqs. (B16), (B20), and (B22) in Appendix B. The solution of Eq. (53) is given by:

$$\mathbf{T}(t_D) = \exp\left(-\mathbf{E}^{-1}\mathbf{F}t_D\right)\int_0^{t_D}\exp\left(-\mathbf{E}^{-1}\mathbf{F}\tau\right)\mathbf{E}^{-1}\mathbf{G}(\tau)d\tau. \tag{54}$$

Substituting Eq. (54) into Eq. (50) yields the final expression for $U(\mathbf{r}_D, t_D)$. The detailed derivation steps leading to this result are presented in Appendix B.

2.6. Assessment of particle trajectories and associated travel times in groundwater flow

The flow trajectories and travel times of water particles within the domain are governed by the advection equation (Ottino, 1989):

$$\frac{\partial \mathbf{r}}{\partial t} = \mathbf{v}(\mathbf{r},\ t), \tag{55}$$

where $\mathbf{v} = (v_x, v_z)$ denotes the Eulerian Darcy velocity components in the horizontal and vertical directions [LT^{-1}], respectively. Since groundwater moves through the pore spaces of an aquifer, the actual particle (pore) velocity must account for the effect of porosity (Bear, 1972):

$$v_{px} = \frac{v_x}{\theta(z)},\ v_{pz} = \frac{v_z}{\theta(z)}, \tag{56}$$

where $\theta(z)$ is the depth-dependent porosity, as defined in Eq. (12).

A particle released from an initial position (x_l, z_l) is advected by the local pore velocity components (v_{px}, v_{pz}). After a time increment Δt, its new position is determined as:

$$x_{l+1} = x_l + v_{px}\Delta t,\ z_{l+1} = z_l + v_{pz}\Delta t. \tag{57}$$

This step is repeated iteratively, updating the particle position at each time interval until the particle exits the domain through the discharge boundary. The total travel time is then obtained as the cumulative sum of all incremental time steps Δt. The sequence of computed positions delineates the particle pathline. In this analysis, the value of Δt is determined through a convergence test to ensure that both the pathline and travel time remain unaffected by further reductions in Δt. Based on this criterion, a time step of 5 days is adopted in the present study.

2.7. Sensitivity analysis

Global Sensitivity Analysis (GSA) was performed to assess the influence of hydrogeological parameters on simulated hydraulic head. Unlike local sensitivity methods, which evaluate the response to small perturbations around a nominal value, GSA quantifies parameter influence across the full input space, capturing both individual effects and higher-order interactions.

The analysis employs the variance-based Innovative Algorithm Estimator proposed by Azzini et al. (2021), which enhances computational efficiency while maintaining the accuracy of sensitivity index estimation. Based on Sobol' variance decomposition (Saltelli et al., 2010), the total variance of the model output Y (hydraulic head) is decomposed into contributions from each parameter and their interactions. The main-effect (S_i) and total-effect (S_{Ti}) sensitivity indices are defined as:

$$S_i = \frac{V(E(Y|X_i))}{V(Y)} \text{ and } S_{Ti} = \frac{E(V(Y|X_{\sim i}))}{V(Y)}, \tag{58}$$

where X_i is the i^{th} input parameter. $X_{\sim i}$ denotes the remaining parameters, $V(\cdot)$ is the variance operator, and $E(\cdot)$ is the expectation operator.

The main-effect index S_i quantifies the fraction of output variance explained solely by parameter X_i. The term $E(Y|X_i)$ represents the conditional mean of the output when X_i is fixed and all other parameters vary over their distributions; the variance of this conditional mean, $V(E(Y|X_i))$, reflects the strength of the main effect (Kumar and Sonkar, 2025).

For the total-effect index S_{Ti}, the term $V(Y|X_{\sim i})$ denotes the conditional variance of the output when all parameters except X_i is fixed. This variance captures the contribution of X_i (including all interactions) to the uncertainty in Y. Taking the expectation $E(V(Y|X_{\sim i}))$ averages this contribution across the full range of the remaining parameters. The denominator $V(Y)$ is the total output variance when all parameters vary simultaneously. A complete description of the numerical procedure used to compute these sensitivity indices is provided in the Supplementary Material S1.

For the present study, the following hydrogeological and pumping parameters were treated as uncertain inputs: $K_{xB_{i-1}}$, $K_{zB_{i-1}}$, A_i, $S_{sB_{i-1}}$, λ_i, and Q_0. This parameter set accounts for aquifer heterogeneity, through depth-decaying hydraulic and storage properties, and external forcing through pumping, enabling a comprehensive sensitivity assessment of hydraulic head dynamics.

2.8. Evaluation of recharge/discharge distribution along the top boundary

The spatial and temporal variation of recharge/discharge along the top boundary is evaluated using the hydraulic head function while accounting for aquifer storage effects, as given by (Zhao et al., 2018):

$$RD(x,\ t) = \left[S_y\frac{\partial h_1}{\partial t} - K_{z1}(z)\frac{\partial h_1}{\partial z}\right]_{z=0}, \tag{59}$$

where S_y denotes the specific yield of the basin at the top boundary [-]. It is important to note that the application of Eq. (59) inherently assumes a linearized free water table boundary, valid under the condition that the recharge/discharge rate is much smaller than the vertical hydraulic conductivity at the surface (Zhang et al., 2022). A positive value of RD indicates recharge, whereas a negative value represents discharge. The computed recharge/discharge function thus quantifies both the spatial extent and temporal evolution of recharge and discharge zones along the aquifer length, governed by periodic fluctuations in the water table boundary.

2.9. Finite time Lyapunov exponent

To further investigate the characteristics of particle motion and mixing within the flow domain, the degree of chaotic behavior was quantified using the finite-time Lyapunov exponent (FTLE). The Lyapunov exponent provides a rigorous measure of the system's sensitivity to initial conditions by describing the rate at which neighboring trajectories diverge. The FTLE quantifies the deformation of an infinitesimal fluid element $d\mathbf{r}(t,\ t_0{:}\ \mathbf{R})$ from its initial configuration $d\mathbf{R} = d\mathbf{r}(t_0,\ t_0{:}\ \mathbf{R})$ as (Trefry et al., 2019):

$$\Lambda(t,\ t_0 : \mathbf{R}) \equiv \frac{1}{2(t-t_0)}\ln v_d, \tag{60}$$

where Λ is the Lyapunov exponent [T^{-1}], $\mathbf{r}$ is the Eulerian frame of reference, $\mathbf{R}$ is the Lagrangian spatial coordinates at initial reference time t_0, v_d is the largest eigenvalue of the Cauchy-Green deformation tensor $\mathbf{C}$:

$$\mathbf{C} = \mathbf{F}(t,\ t_0 : \mathbf{R})^{\mathrm{T}}\cdot\mathbf{F}(t,\ t_0 : \mathbf{R}). \tag{61}$$

Here, $\mathbf{F} \equiv \frac{\partial \mathbf{r}}{\partial \mathbf{R}}$ is the deformation gradient tensor.

A positive Lyapunov exponent ($\Lambda > 0$) signifies exponential trajectory divergence and chaotic advection, $\Lambda < 0$ denotes convergence and stability, and $\Lambda = 0$ corresponds to a marginally stable or neutral state. Further theoretical insights into the FTLE framework can be found in Trefry et al. (2019).

In practical groundwater flow applications, trajectory data are available only over finite time intervals; hence, the FTLE is computed. The FTLE characterizes local stretching and separation of fluid trajectories over a finite integration time and serves as a diagnostic measure to identify transport barriers, coherent flow structures, and regions of enhanced mixing within the subsurface flow domain.

3. Results and discussions

This section is divided into two subsections. Subsection 3.1, Verification of the developed model, presents the validation of the proposed analytical model through comparison with existing analytical and numerical solutions. Subsection 3.2, Discussion, explores the variations in pathlines, chaotic advection, and parameter sensitivity derived from the proposed formulation. The parameter values used in the analysis are summarized in Table 1 and Table C1 and are not reiterated unless modifications are introduced for specific cases.

3.1. Verification of the developed model

The proposed analytical model is validated through comparison with the model developed by Zhao et al. (2018). While Zhao's model assumes a simplified single-layer aquifer with uniform hydraulic conductivity and specific storage, the proposed model accounts for a three-layer aquifer system characterized by depth-dependent hydraulic properties

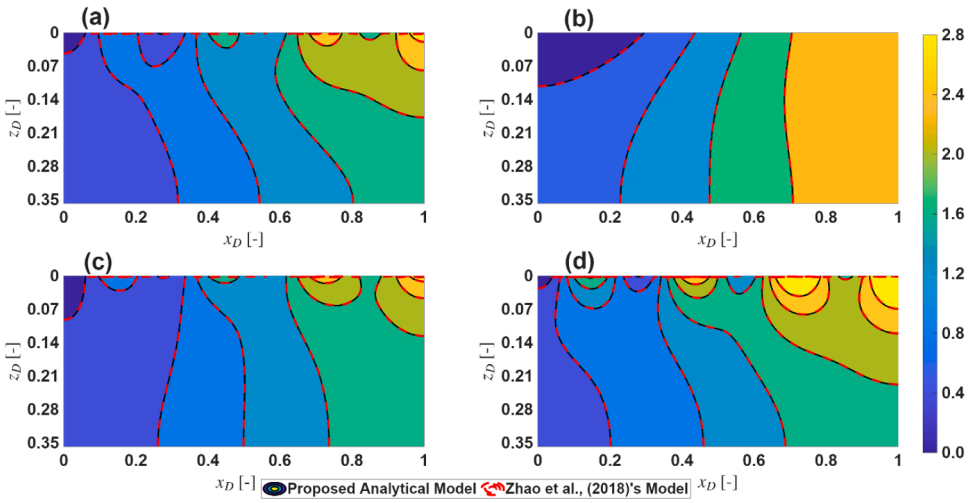

Fig. 3. Comparison of the dimensionless hydraulic head contour lines obtained from the proposed analytical model and the model of Zhao et al. (2018) at four time instances: (a)0.25P, (b)0.50P, (c)0.75P, and (d) 1.00P. In Zhao's model, the aquifer parameters are specified as $L = 7000$ m, $B = 2500$ m, $K_x = K_z = 1$ m/d, and $S_s = 0.0001$ m^{-1}.

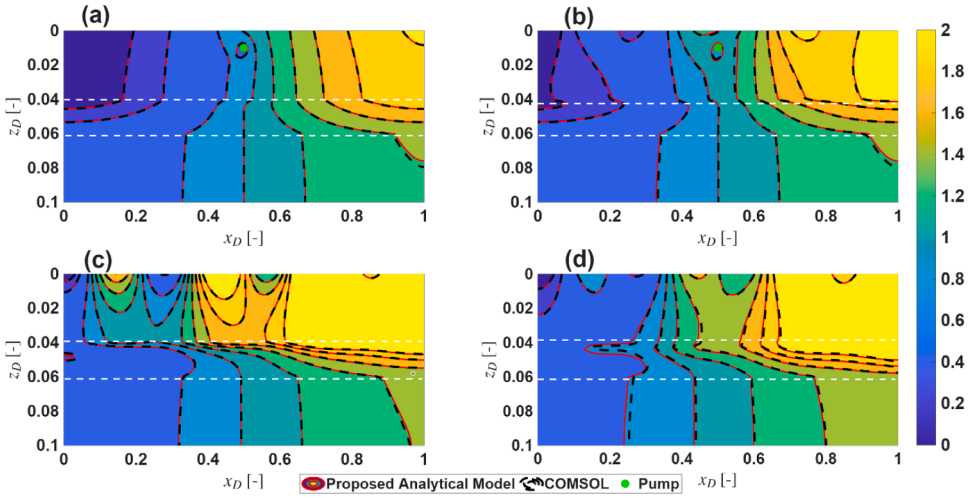

Fig. 4. Comparison of dimensionless hydraulic head contour profile obtained from the proposed analytical solution and the COMSOL Multiphysics finite element model at different time instances: (a)0.04P, (b)0.164P, (c) 0.50P, and (d) 0.75P.

under pumping condition. For validation, the parameterization of the proposed model is tailored to replicate Zhao's assumptions. Specifically, the decay coefficients in all layers are assigned sufficiently small values so that the exponential terms in the hydraulic conductivity expression converge to unity, thereby producing constant hydraulic conductivity throughout the system. Hydraulic conductivity is fixed at 1 m/d across all layers. Similarly, residual specific storage is set to 1×10^{-5} m^{-1}, the specific storage at the top of each layer to 1×10^{-4} m^{-1}, and the decay index of specific storage to zero. These settings ensure that specific storage remains constant throughout the domain, consistent with Zhao's formulation. In addition, the boundary condition is modified by replacing the $\sin^2\left(\pi \frac{t}{P}\right)$ term with $\cos^2\left(\pi \frac{t}{P}\right)$, aligning with Zhao's use of the cosine function at the top boundary.

Fig. 3 compares the dimensionless hydraulic head contours obtained from the proposed model and from Zhao et al. (2018) at four-time instances: 0.25P, 0.50P, 0.75P, and 1.00P. The two models exhibit strong agreement overall, with minor deviations near the top boundary. This discrepancy arises because Zhao's formulation separates the solution of the governing equation into two components: a steady-state solution that represents the regional groundwater table at the top boundary, and a transient solution that imposes seasonal fluctuations of the local water table at the surface under a zero-head initial condition. The transient solution was obtained via Laplace transformation, followed by inversion to recover the temporal response. While this methodology successfully captures the influence of temporal hydraulic head variability on the aquifer, but it does not reproduce boundary variations exactly at the surface. A detailed discussion of this limitation is provided in Das and Sarmah (2025). Notably, the discrepancy vanishes at $t = 0.50P$, when the cosine term in the boundary condition reduces to zero, eliminating local head variations and leaving only the regional component.

The analytical solution was further validated through cross-comparison with the corresponding numerical solution of the flow problem, obtained using COMSOL Multiphysics based on the finite element method. The flow domain was discretized using a mesh with a maximum element size of 5 m and a minimum element size of 0.2 m, and the maximum time step was set to 1 day. Time integration was performed using the Backward Differentiation Formula (BDF), a multi-step implicit scheme that advances the solution by solving a system of equations based on a backward-weighted average of previous time steps. The BDF method is particularly suited for stiff problems, systems of differential equations in which certain components evolve much more

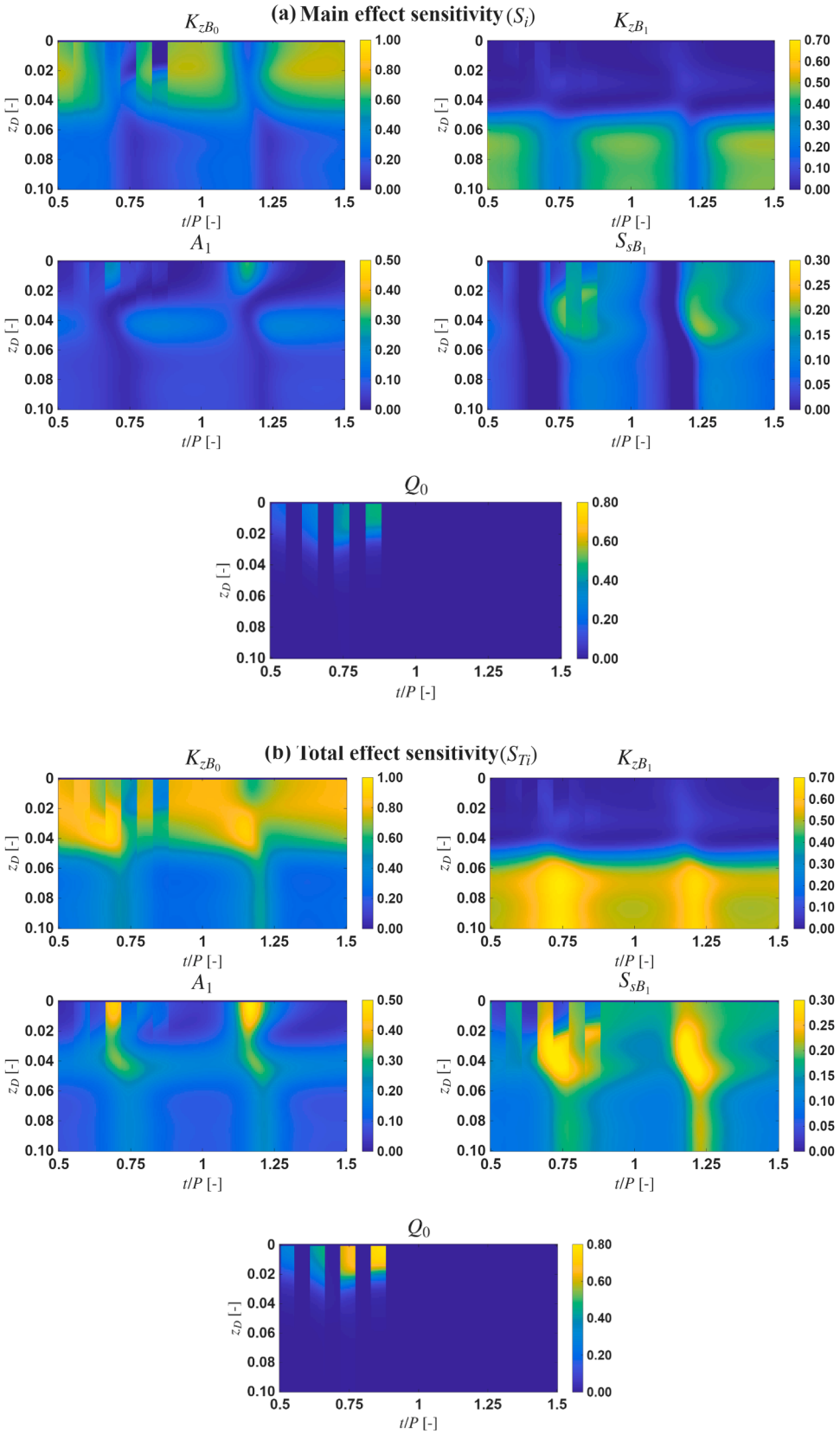

Fig. 5. Temporal variation of global sensitivity indices of hydraulic head along vertical profiles at the horizontal mid-span ($x_D = 0.50$) of the flow domain: (a) Main-effect sensitivity indices (S_i), (b) Total-effect sensitivity indices (S_{Ti}).

rapidly than others, such as those commonly encountered in heat transfer and groundwater flow. To handle this stiffness, adaptive time stepping was employed, allowing the time step size to automatically adjust for numerical stability and computational efficiency.

Fig. 4 presents the dimensionless hydraulic head contour plots from both the analytical and numerical models at four different time instances: 0.04P,0.164P,0.50P, and 0.75P. The red contour lines denote the analytical solution, while the black dotted lines represent the COMSOL-based numerical solution. A pumping well, located at $x_{D0} = 0.5$ and $z_{D0} = 0.01$ (marked as a green dot in the figure), was operated intermittently, 20 days of pumping followed by 20 days of rest, in an alternating pattern for a total period of 140 days from the initial reference time, at a discharge rate of 100 m^2/d. The contours demonstrate that the numerical solution closely reproduces the spatial and temporal trends of the analytical solution. The values of the model parameters used in this analysis are summarized in Table 1 and Table C1.

3.2. Discussions

3.2.1. Global sensitivity analysis of hydraulic head function

The sensitivity of the dimensionless hydraulic head was analyzed with respect to several key parameters, including horizontal and vertical hydraulic conductivity, hydraulic conductivity decay coefficients, specific storage at the top surface of the layers, specific storage fitting coefficients, and the pumping rate. The parameter ranges considered in this analysis are as follows: $K_{xB_0} \in [5\ 50]$, $K_{xB_1} \in [0.01\ 5]$, $K_{xB_2} \in [1\ 11.15]$, $K_{zB_0} \in [0.5\ 5]$, $K_{zB_1} \in [0.001\ 0.5]$, $K_{zB_2} \in [0.1\ 1.11]$, $A_1 \in [0.0001\ 0.005]$, $A_2 \in [0.0001\ 0.005]$, $A_3 \in [0.0001\ 0.005]$, $S_{sB_0} \in [0.00001\ 0.0005]$, $S_{sB_1} \in [0.0001\ 0.005]$, $S_{sB_2} \in [0.00001\ 0.000021]$, $S_{sr1} \in [0.000001\ 0.00001]$, $S_{sr2} \in [0.00001\ 0.0001]$, $S_{sr3} \in [0.000001\ 0.00001]$, $\lambda_1 \in [9\ 20]$, $\lambda_2 \in [9\ 20]$, $\lambda_3 \in [9\ 20]$ and $Q_0 \in [0\ 100]$. These parameter ranges are consistent with field-observed values (Jiang et al., 2009; Cai et al., 2023; Das et al., 2026; Kuang et al., 2021; Zhuang et al., 2024).

Parameter sampling was performed using MATLAB's built-in 'sobolset' function, which generates quasi-random (QR) Sobol sequences. QR Sobol sequences provide superior, space-filling coverage of the p-dimensional unit hypercube compared to traditional Monte Carlo sampling, as each successive point reduces gaps in the existing distribution (Saltelli et al., 2010). To further enhance uniformity and reduce structural artifacts, MATLAB's 'scrambled' function was used using MatousekAffineOwen scheme (Hong et al., 2003). The QR samples in the unit hypercube were then linearly mapped to the physical parameter ranges using their respective minimum and maximum bounds.

A total of 19 parameters were included in the sensitivity analysis. A uniformly distributed sample of 1,000 data points was generated for each parameter. The total computational cost of the analysis can be expressed as $2n(p + 1)$, where n represents the number of samples and p the number of parameters, yielding a total cost of 40,000 model evaluations in this study. The detailed methodology used to compute the global sensitivity indices is described in sub-section 2.7.

Fig. 5a and b illustrates the variation of global sensitivity indices of hydraulic head over time along vertical profiles located at the horizontal mid-span ($x_D = 0.5$) of the flow domain. This location was selected because the influence of the lateral no-flow boundaries at $x_D = 0$ and $x_D = 1$ is minimal at the mid-span, ensuring that the sensitivity results are not biased by boundary effects. Moreover, the mid-span lies sufficiently close to the pumping well located at (x_{D0}, z_{D0}) = (0.51, 0.01), enabling the sensitivity analysis to capture the combined effects of periodic recharge and localized pumping stresses without being dominated by boundary-induced artefacts.

Fig. 5(a) presents the main-effect sensitivity indices (S_i), which quantify the contribution of each parameter to the variability of the output, while Fig. 5(b) shows the total-order sensitivity indices (S_{Ti}), which capture the combined influence of both the individual effects of each parameter and their interactions with other parameters.

The analysis was conducted over the interval between two consecutive peak water table configurations to represent conditions between successive monsoon events, with the water table attaining its maximum levels at 0.5P and 1.5P. Pumping commenced at 0.5P and followed an alternating pattern of 20 days of pumping and 20 days of rest, continuing for a total of 140 days from the start of pumping. This configuration allowed evaluation of how transient recharge and episodic pumping jointly influence parameter sensitivities in the system.

In this study, the discussion primarily focuses on parameters for which the sensitivity of the dimensionless hydraulic head is significant, defined as having total sensitivity indices (S_{Ti}) greater than 0.2. The analysis revealed that the hydraulic head is most sensitive to variations in K_{zB_0}, K_{zB_1}, A_1, S_{sB_1}, and Q_0, whereas the remaining flow parameters exhibit low to mild sensitivity, with S_{Ti} values below 0.2.

From the analysis, it is evident that the hydraulic head is sensitive to the top-surface vertical hydraulic conductivity values of the first and second layers. The top-surface vertical conductivity of the first layer (K_{zB_0}) predominantly influences the hydraulic head within the upper layer, with its impact diminishing progressively with depth and becoming minimal in the bottom layer. However, under pumping conditions, the sensitivity to K_{zB_0} varies depending on the position of the water table boundary. At $t = 0.5P$, when the water table reaches its maximum elevation and pumping begins, the hydraulic head exhibits high sensitivity to K_{zB_0} and relatively low sensitivity to the discharge rate (Q_0). As t progresses towards P, the water table concurrently continues to recede, leading to increased sensitivity of the hydraulic head to Q_0 during the pumping period, and reduced sensitivity to vertical hydraulic conductivity K_{zB_0}, as shown in Fig. 5a and b. This behavior is attributed to the reduction in hydraulic head gradients as the water table declines; during such periods, the gradient induced by pumping becomes more dominant than the gradient driven by water table fluctuations.

The dimensionless hydraulic head exhibits the highest sensitivity to the top-surface vertical conductivity of the second layer (K_{zB_1}) within the bottom layers, while showing minimal sensitivity in the top layer. Temporally, within the bottom layers, the main-effect sensitivity to K_{zB_1} is lowest around $t = 0.75P$ and $t = 1.25P$. However, the total-order sensitivity is highest at these times, indicating a substantial contribution of interaction effects, where other flow parameters act in combination with K_{zB_1} to influence the hydraulic head, as observed in Fig. 5b. The pumping effect on sensitivity to K_{zB_1} is almost negligible throughout the domain.

The hydraulic conductivity decay coefficient of the first layer (A_1) exhibits strong main-effect sensitivity within the upper 200 m of the domain, particularly around $t = 0.75P$ and $t = 1.25P$, and shows a moderate effect in the second layer at all times except at these two instances (refer to Fig. 5a). Given the substantial variation in conductivity with depth in the upper 200 m, the sensitivity is primarily concentrated in this zone. Under pumping conditions, the sensitivity to A_1 becomes negligible, as indicated by the nearly vanishing main-effect and total-effect responses.

The top surface specific storage of the middle layer (S_{sB_1}) exhibits moderate sensitivity to the hydraulic head in the top and middle layers, and weak sensitivity in the bottom layer. Under pumping conditions, its

Table 2
Model parameters with their lower and upper bounds, and average values used in the MCS uncertainty analysis.

Parameters	Lower bound	Upper bound	Average value	Units
K_{xB_0}	5	50	10	m/d
K_{xB_1}	0.01	5	0.05	m/d
K_{zB_0}	0.5	5	1	m/d
K_{zB_1}	0.001	0.5	0.01	m/d
S_{sB_0}	0.00001	0.0005	0.0001	m^{-1}
S_{sB_1}	0.0001	0.005	0.001	m^{-1}
Q_0	0	100	50	m^2/d

influence diminishes within the upper 200 m, reducing the sensitivity to nearly zero. The total sensitivity response is pronounced across the spatio-temporal domain, with peaks near $t = 0.75P$ and $t = 1.25P$, as evident in Fig. 5b. The elevated sensitivity spanning the first and second layers suggests that the storage capacity of the middle layer significantly influences hydraulic head variations in the overlying layers.

The hydraulic head exhibits high sensitivity to the pumping discharge rate (Q_0), particularly during the pumping intervals in the vicinity of the pump location. With successive pumping cycles, this sensitivity increases progressively. The total sensitivity is enhanced by approximately 70 % compared to the main effect, primarily due to strong interaction effects with other flow parameters, which collectively amplify the influence of pump discharge on the hydraulic head response.

It should be noted that in Fig. 5(a-b), the sensitivity fields display noticeable non-smooth variations at certain time intervals. This behavior can be attributed to two main factors. First, the imposed water-table boundary condition follows a sinusoidal function, which inherently introduces periodic changes in slope. At the inflection points of the sinusoid, approximately at $t \approx 0.75P$ and $t \approx 1.25P$, the slope of the boundary head reverses direction, leading to abrupt transitions in the governing vertical gradients. These instants correspond to moments when the rate of change of the water-table fluctuation is minimal (during the falling limb near $t \approx 0.75P$) or maximal (during the rising limb near $t \approx 1.25P$), causing the main-effect sensitivities to diminish or approach zero.

Second, an additional source of irregularity arises between $0.50P$ and $1.00P$ due to intermittent pumping. The on-off pumping schedule interacts with the periodic boundary signal, intensifying nonlinear parameter interactions. As a result, the total-effect sensitivities remain significant during these intervals, even when the main-effect sensitivities are reduced. This combination of transient boundary forcing and parameter interaction naturally leads to the non-smooth patterns observed in the sensitivity plots.

3.2.2. *Model uncertainty analysis*

Stochastic simulation was employed to quantify the uncertainty in model predictions arising from variability in input parameters, which is largely attributed to the geological heterogeneity of subsurface formations. In this study, uncertainty analysis was conducted to assess the influence of parameter variability, specifically hydraulic conductivity, specific storage, and pumping rate, on the simulated hydraulic head values, as these parameters exert a dominant control on subsurface flow. Previous studies (Govindaraju and Koelliker, 1994; Hoeksema et al., 1985; Srivastava et al., 2002; Zhao and Illman, 2021) have reported that both hydraulic conductivity and specific storage typically follow a log-normal distribution, which aligns with the assumptions adopted in

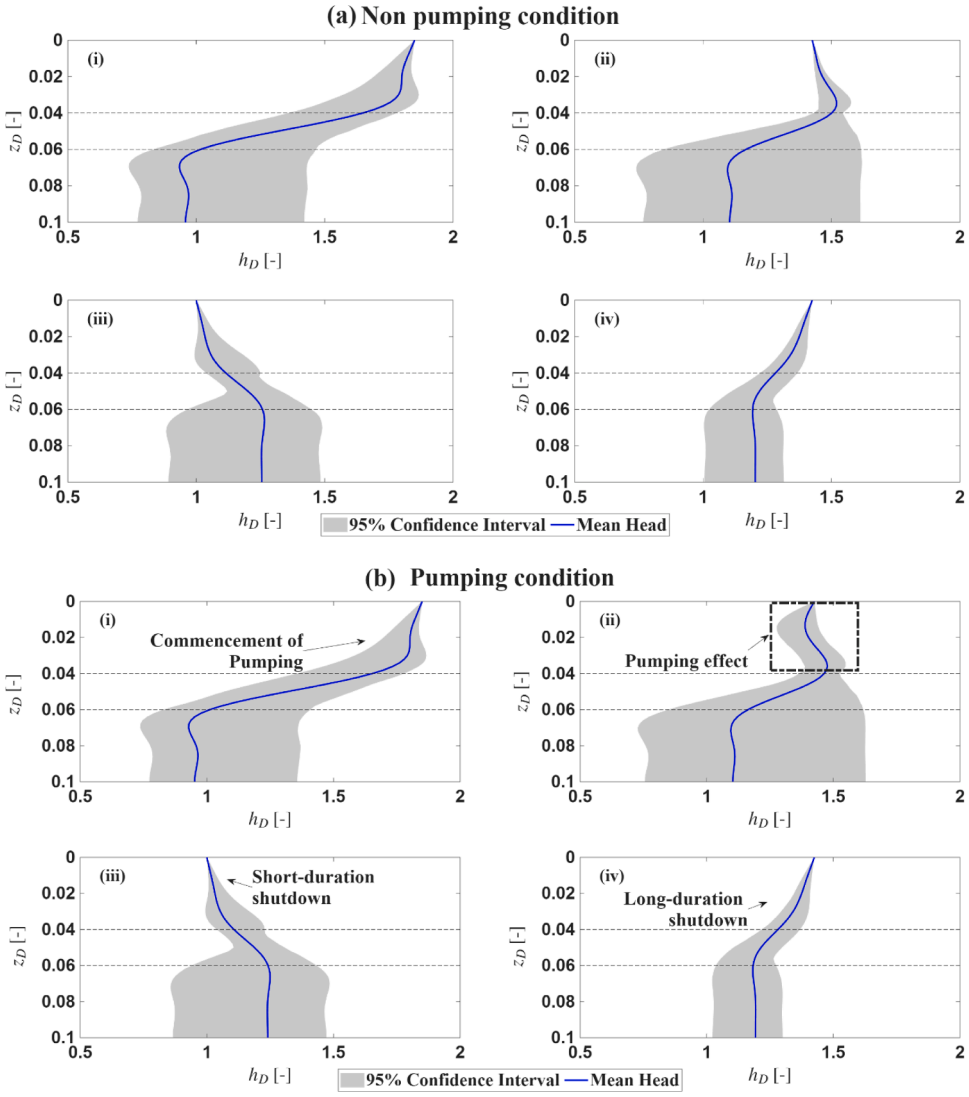

Fig. 6. Depth-wise variability of the dimensionless hydraulic head at $x_D = 0.50$ at four selected time instances under (a) non-pumping and (b) pumping conditions. The solid blue line represents the mean head, while the shaded region represents the 95 % confidence interval.

this study, while pumping rate was assumed to follow a normal distribution. A Monte Carlo Simulation (MCS) framework was used to incorporate spatial variability in these parameters and evaluate their impact on model outputs. The uncertainty in output variables was quantified using a non-parametric bootstrap technique (Efron, 1979). Across the three layers, ten parameters ($K_{xB_{i-1}}$, $K_{zB_{i-1}}$, $S_{sB_{i-1}}$, Q_0) were defined based on their 95 % distribution bounds, and approximately 1, 000 realizations were generated for each, as summarized in Table 2.

The hydrogeological properties of the first and bottom layers were assumed to be identical, considering both represent the same geological formation; therefore, the same depth-decaying trends in hydraulic conductivity and specific storage used for the first layer were extended to the bottom layer. Input parameter data for the MCS were generated using the upper, and bottom values (Table 2) based on their respective probability distributions at the layer surfaces. The parameter fields over the full depth domain were then obtained by applying the specified depth-decay relationships for hydraulic conductivity and specific storage [Eqs. (13)-(16)].

Model output variability in dimensionless hydraulic head (h_D) was evaluated at $x_D = 0.5$ along the full depth at four time instances: $t = 0.50P$, $0.75P$, $1.00P$, and $1.25P$. These time steps correspond to the imposed pumping schedule, which begins at $t = 0.50P$ and alternates between 20 days of operation and 20 days of shutdown, continuing until $= 0.884P(\approx 140\text{days})$. This time window captures both active pumping and recovery phases, enabling the assessment of variability during and after pumping events.

Fig. 6a presents the 95 % confidence intervals of dimensionless hydraulic head variability at four time instances: (i) $0.50P$, (ii) $0.75P$, (iii) $1.00P$, and (iv) $1.25P$. The results indicate that across all water table positions, the maximum head variability occurs in the bottom layer under both pumping and non-pumping conditions, with variability increasing with depth. At the surface, head variability is zero due to the water table boundary, whose magnitude remains invariant to aquifer properties. Moving downward from the surface, the influence of this boundary diminishes, leading to progressively greater uncertainty in the predicted hydraulic head. Additionally, the uncertainty in head predictions amplifies within the middle layer, which is attributed to its relatively higher specific storage compared to the other layers. A higher specific storage enhances the capacity of the layer to store and release water, thereby increasing its potential to modulate head variability under a broad spectrum of hydrogeological properties.

The influence of pumping is illustrated in Fig. 6b. Pumping begins at $t = 0.50P$ operates intermittently until $t = 0.884P$. The effect is most pronounced at $t = 0.75P$, during the active pumping interval, where the mean head decreases near the pumping location and the variability increases. Outside the pumping period, head variability remains largely unchanged.

3.2.3. Recharge/discharge variation along the top boundary

The spatial distribution of recharge and discharge along the upper boundary reflects the continuous seasonal fluctuations of the water table, which cause both the location and magnitude of vertical fluxes to vary over time. To evaluate how these zones respond under varying hydrogeological conditions, three hydraulic configurations are examined: (i) depth-decaying hydraulic parameters without pumping, (ii) equivalent hydraulic parameters without pumping, and (iii) depth-decaying hydraulic parameters with pumping.

The first configuration incorporates the vertical variation of hydraulic conductivity and specific storage as described in Eqs. (13)-(15), with the pumping rate set to zero ($Q_0 = 0$). In the equivalent homogeneous case, each layer is assigned constant hydraulic properties. The equivalent vertical hydraulic conductivity $\left(K_{zi}^{eq}\right)$ is computed using the harmonic mean, whereas the equivalent horizontal hydraulic conductivity $\left(K_{xi}^{eq}\right)$ and specific storage $\left(S_{si}^{eq}\right)$ are determined using arithmetic means (Das et al., 2026), expressed as $\frac{1}{K_{zi}^{eq}} = \frac{1}{(B_i - B_{i-1})} \int_{B_{i-1}}^{B_i} \frac{1}{K_{zi}(z)} dz$, $K_{xi}^{eq} = \frac{1}{(B_i - B_{i-1})} \int_{B_{i-1}}^{B_i} K_{xi}(z) dz$ and $S_{si}^{eq} = \frac{1}{(B_i - B_{i-1})} \int_{B_{i-1}}^{B_i} S_{si}(z) dz$. The third configuration is identical to the first in terms of aquifer heterogeneity but includes a nonzero pumping rate to assess its influence on the recharge/discharge dynamics. Pumping commences at $t = 0.75P$ and continues for a duration of $0.50P$, after which the well was shut down at $1.25P$; this cycle repeats annually. The pumping well is located at coordinates (1550, 200) m. The procedure for evaluating the recharge/-discharge function is detailed in Sub-section 2.8.

A positive value of the recharge/discharge function ($RD > 0$) represents recharge, whereas a negative value ($RD < 0$) indicates discharge. For the analysis, four representative time steps, (a) $0.75P$, (b) $1.00P$, (c) $1.25P$ and (d) $1.50P$, are considered to delineate the temporal evolution of recharge and discharge zones. In the corresponding figures, the dashed grey lines depict the temporal fluctuations of the water table.

The results show that the magnitude of recharge and discharge is consistently higher in the depth-decaying hydraulic-conductivity configuration than in its equivalent homogeneous counterpart (Fig. 7a–c). Because the equivalent model uses depth-averaged properties, it assigns lower hydraulic conductivity near the surface and higher values at depth relative to the depth-decaying profile. Since the recharge/discharge function is evaluated along the upper boundary, where the depth-decaying profile attains its highest conductivity, the

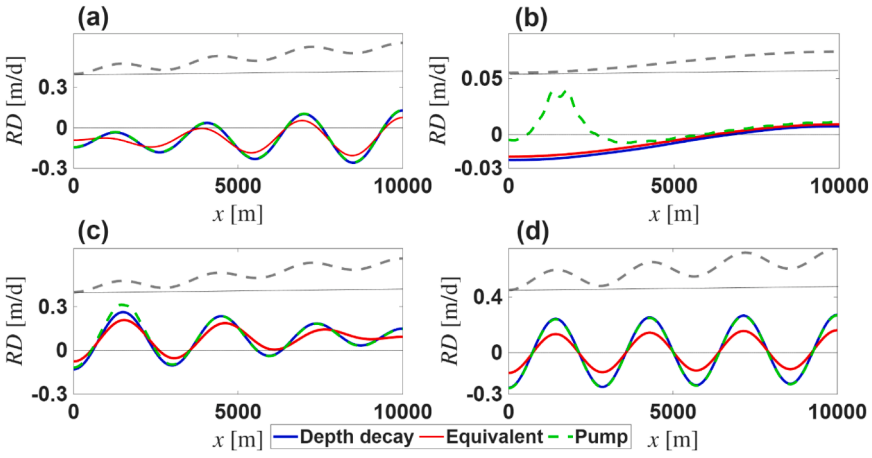

Fig. 7. Spatial variation of the recharge/discharge (RD) function along the top boundary under heterogeneous and equivalent homogeneous aquifer conditions, with and without pumping, shown at different simulation times: (a) $0.75P$, (b) $1.00P$, (c) $1.25P$, and (d) $1.50P$. The gray dashed line represents the water table boundary.

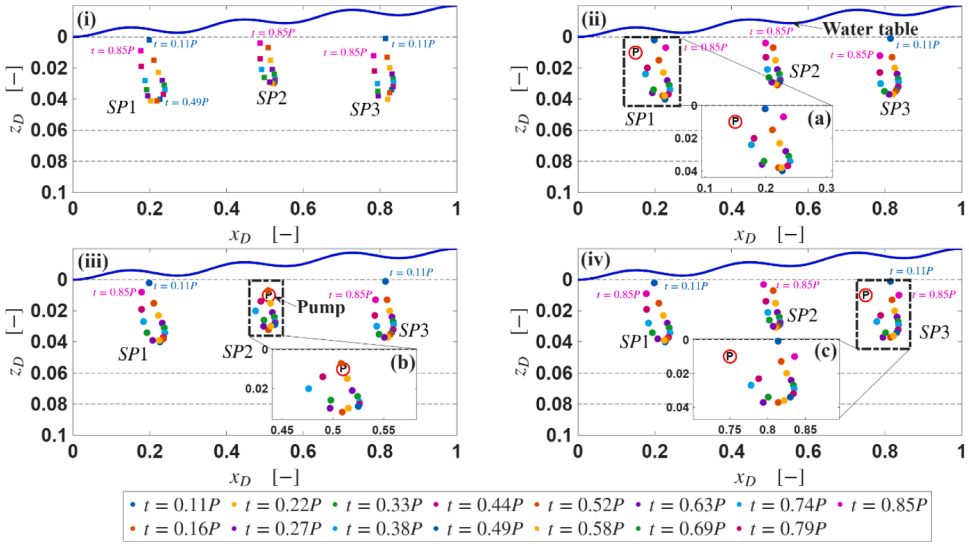

Fig. 8. Comparison of stagnation zones SP1-SP3 under no pumping (i), and three pumping configurations (ii–iv). Wells are placed at (0.1500, 0.010), (0.5100, 0.010) m, and (0.7500, 0.010). Zoomed panels (ii)-a to (iv)-c highlight the distortion of loop and lateral displacement of stagnation points produced by water-table oscillations and pump-induced horizontal fluxes. Blue curve represents the water table.

depth-decaying configuration produces stronger vertical fluxes. In contrast, the homogenized model underestimates near-surface conductivity and therefore yields weaker recharge and discharge magnitudes.

During the low water-table phase (typically post-monsoon), much of the domain functions as a discharge zone. Storage-induced lag causes the deeper portions of the aquifer to retain higher hydraulic head from earlier high-water-table conditions, generating upward vertical gradients and enhanced discharge toward the surface. Pumping intensifies this response by further lowering the local water-table head, generating sharp recharge peaks near the well as water is drawn downward (refer to Fig. 7b). This influence is subdued during high water-table conditions, when regionally driven hydraulic gradients exceed the localized drawdown effects, limiting the pumping radius of influence and reducing the contrast between pumping and non-pumping cases. Once pumping ceases, its effect is rapidly overridden by ongoing water-table fluctuations and the elevated upstream hydraulic head, which restore the regional flow field and diminish residual pumping-induced anomalies.

3.2.4. *Evolution of stagnation points*

The analysis of stagnation points is important in hydrogeology because they exert a strong control on groundwater residence times, mixing efficiency, and transport pathways. In transient flow systems driven by periodic water-table fluctuations, true stagnation points, defined by exactly zero velocity, do not always persist. Instead, locations where the resultant velocity attains a local minimum are commonly observed and are referred to here as pseudo-stagnation points. Under steady-state conditions, both stagnation and pseudo-stagnation points remain fixed in space, whereas under transient forcing their positions may migrate, appear, or disappear over time (Zhang et al., 2025).

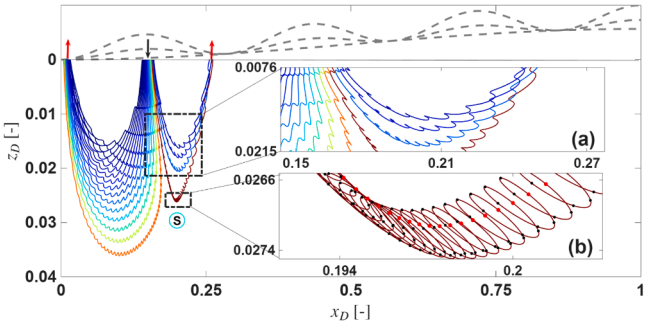

Fig. 9. Particle trajectories under a fluctuating water table considering aquifer specific storage. Insets (a) and (b) provide magnified views highlighting path curvature and intermediate particle positions at two different locations.

As the water table oscillates, these stagnation points undergo periodic migration, often tracing loop-like trajectories, creating zones of very low resultant velocity in which fluid particles can remain for extended durations. Similar stagnation-point dynamics have been reported under a range of hydrogeological settings (Das et al., 2026; Das and Sarmah, 2025; Zhang et al., 2025; Zhao et al., 2018). In the present study, we specifically examine how pumping perturbs the location and evolution of these stagnation points under transient boundary forcing.

Fig. 8 compares the temporal variation of stagnation points for four cases: a no-pumping scenario [Fig. 8(i)] and three pumping configurations in which wells are placed near identified stagnation zones SP1, SP2, and SP3 [Fig. 8 (ii–iv)]. The corresponding pumping locations are (0.1500, 0.010), (0.5100, 0.010), and (0.7500, 0.0100), respectively, with pumping schedules identical to those described in Section 3.2.1. The zoomed panels [Fig. 8(ii)-a to 8(iv)-c] highlight the distortions and shifts of the stagnation points induced by pumping.

At the start of the simulation, when the water table is at its minimum elevation, stagnation points are absent. As the water table rises, the downward displacement of the vertical zero-flux contour caused by increasing hydraulic head leads to the formation of stagnation points along the upper-right side of each zone. These points reach their maximum depth at peak water-table elevation ($t \approx 0.5P$) and subsequently move upward as the water table declines and vertical hydraulic gradients weaken.

Pumping significantly modifies these migration pathways by dislocating the stagnation points. In the no-pumping case, the stagnation point at $t = 0.85P$ appears on the upper-left side of the zone, whereas the introduction of a nearby pumping well shifts the point toward the right, driven by the enhanced horizontal hydraulic gradients induced by pumping. Similar behavior is observed in the other pumping configurations. Notably, the migration is not uniformly directed away from the pumping wells; at intermediate times (e.g., $t = 0.63P$ and $t = 0.74P$), some stagnation points move toward the wells. This behavior reflects the complex interplay between locally enhanced horizontal fluxes and the evolving vertical head distribution imposed by transient boundary conditions.

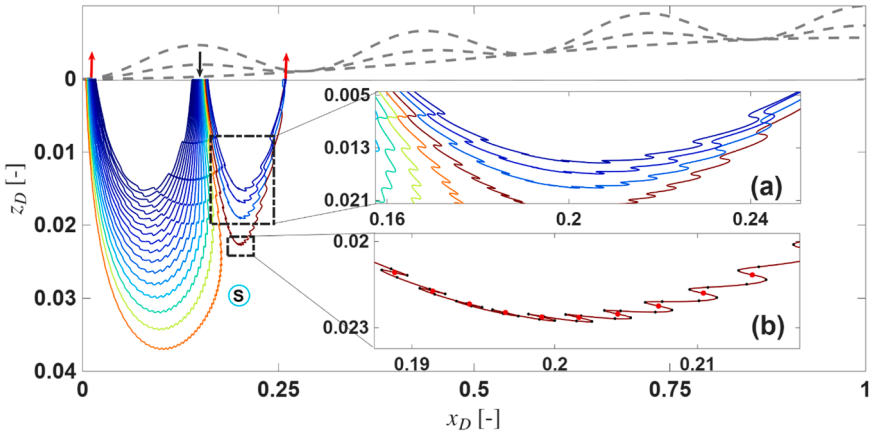

Fig. 10. Particle trajectories under a fluctuating water table neglecting the aquifer specific storage. Insets (a) and (b) provide magnified views highlighting path curvature and intermediate particle positions at two different locations.

3.2.5. *Particle flow dynamics influenced by water table fluctuations, specific storage and pumping*

Seasonal fluctuations of the water table and the aquifer's specific storage strongly influence particle flowpaths within the basin. Pathlines and associated travel times were computed using advective transport along the pore network, as outlined in Sub-section 2.6. Figs. 9 and 10 illustrate particle trajectories for two conditions: (a) when aquifer storage effects are included and (b) under a quasi-steady assumption where storage is neglected. Colored curves depict particle trajectories, while dashed grey curves indicate seasonal variations in the water table. The specific storage is generally understood as a parameter defining ability of the aquifer to store/release water under head change, however, its influence on pathline dynamics remains insufficiently explored in the literature.

To examine the role of specific storage on pathline behavior, water particles were released from the recharge zone ($RD > 0$)at 10 m intervals between 1400 m and 1600 m. At the initial time, when the water table corresponds to the regional minimum configuration, the entire top boundary acts as a discharge zone (Das and Sarmah, 2025; Zhao et al., 2018). Therefore, particle release was initiated with a lag of 73 days from the initial condition. To delineate the particle positions along the pathline under varying water table configurations, a zoomed-in view of the trajectory originating from (1570, 0) m is shown in the inset marked as panel (b). The red dots correspond to the minimum water table configurations obtained at 365-day intervals, while the black dots represent intermediate positions between successive red dots, subdivided into five equal time steps of 73 days each, highlighting the seasonal evolution of the pathline.

The analysis indicates a lateral divergence of flow trajectories, with pathlines bifurcating toward opposite discharge zones when released from (1560, 0) m and (1570, 0) m. Particles introduced between $x =$ 1400-1560 m migrate toward the left discharge zone, whereas those released between $x =$ 1570-1600 m advance toward the right discharge zone, as shown in Figs. 9 and 10. The bifurcation of pathlines in opposite directions leads to the formation of a zone characterized by near-zero directional velocity components, denoted as S, representing a pseudo-stagnation zone. Pathlines passing near S slow substantially, with both horizontal and vertical velocities decreasing, causing particles to remain in the vicinity for extended periods (years, as indicated by red dots). Within each year, seasonal water table fluctuations induce alternating vertical velocities, resulting in moving spiral motion of the pathlines near S. This spiral criss-crossing is densest near S and diminishes with distance.

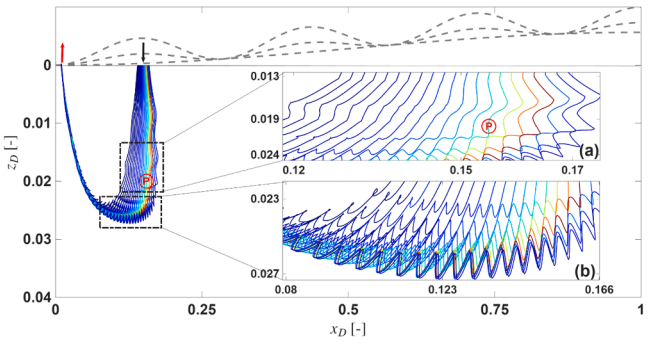

Fig. 11. Particle trajectories under a fluctuating water table considering the effect of aquifer pumping. Insets (a) and (b) provide magnified views highlighting path curvature.

The water table oscillates continuously between its maximum and minimum elevations, causing the hydraulic head throughout the aquifer to fluctuate correspondingly. These boundary-driven fluctuations induce alternating vertical velocities: downward fluxes dominate when the water table is elevated, upward fluxes occur when the water table drops to its minimum, and transitional phases occur in between (Das and Sarmah, 2025; Zhao et al., 2018). The specific storage of the aquifer governs how these fluctuations propagate into the subsurface by introducing a temporal lag between boundary forcing and internal hydraulic response.

When S_s is appreciable, the aquifer retains a portion of the hydraulic head from the previous boundary state. Thus, when the water table reaches its minimum position, the aquifer still maintains comparatively higher head values, resulting in stronger upward vertical fluxes. This short-duration but intensified upward flow periodically deflects particle trajectories upward from their main flow direction, generating pronounced wavy patterns, as observed in Fig. 9. In contrast, when storage is negligible, hydraulic head changes within the aquifer occur almost instantaneously in response to boundary oscillations. The resulting upward vertical flux is brief and weak, as the aquifer no longer retains excess head during periods of falling water table. Consequently, pathlines show only mild, smooth undulations and do not exhibit spiral or intersecting patterns (as seen in Fig. 10). In this case, the trajectories are governed solely by the imposed boundary oscillation, without the additional complexity introduced by delayed hydraulic response.

The influence of pumping on pathline dynamics was further examined by placing a pumping well at (1550, 200) m. Pumping commenced at 273.75 days and continued continuously for 182.5 days (until 456.25 days), coinciding with the lowest water table period. This pumping cycle was repeated annually for 30 years. Particles were released from the same recharge locations ($x =$ 1400–1600 m) as in the previous cases.

Pumping substantially alters the particle trajectories compared to natural conditions. Under unstressed conditions, particles bifurcate

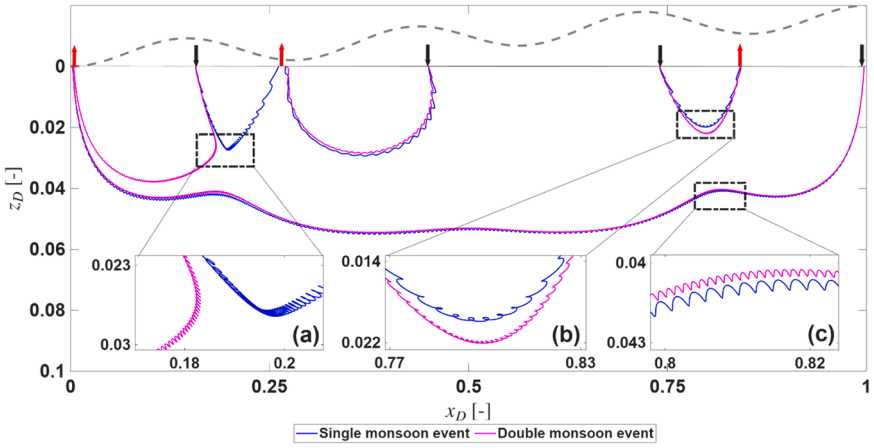

Fig. 12. Simulated particle flow trajectories corresponding to single and dual monsoon events. Insets (a), (b) and (c) provide magnified views highlighting path curvature.

around the pseudo-stagnation zone *S*; however, continuous pumping generates a strong and persistent head gradient that redirects particles predominantly toward the left discharge boundary, as observed in Fig. 11. The induced downward draw causes particles that would have moved toward the right valley to instead descend vertically, effectively eliminating the pseudo-stagnation zone. Once particles are pulled downward, the regional gradient, from the upstream summit toward the downstream valley, advects them laterally toward the right discharge boundary. Since stagnation or pseudo-stagnation zones are regions of very low velocity, sustained pumping can re-activate these inert regions, mobilizing long-residing particles toward nearby surface-water bodies, which may pose environmental risks. Moreover, the characteristic wavy oscillations seen in natural trajectories disappear under pumping, replaced by more linear paths. The spiral motion near *S* also vanishes, demonstrating that prolonged anthropogenic stress overrides the natural oscillatory dynamics imposed by the fluctuating water table and reshapes the local head field.

3.2.6. *Influence of the bimodal monsoon on particle trajectories*

The monsoon regime exerts a substantial influence on groundwater flow behavior and particle trajectories in both surface and subsurface flow systems. Nicholson et al. (2013, 2018) documented the occurrence

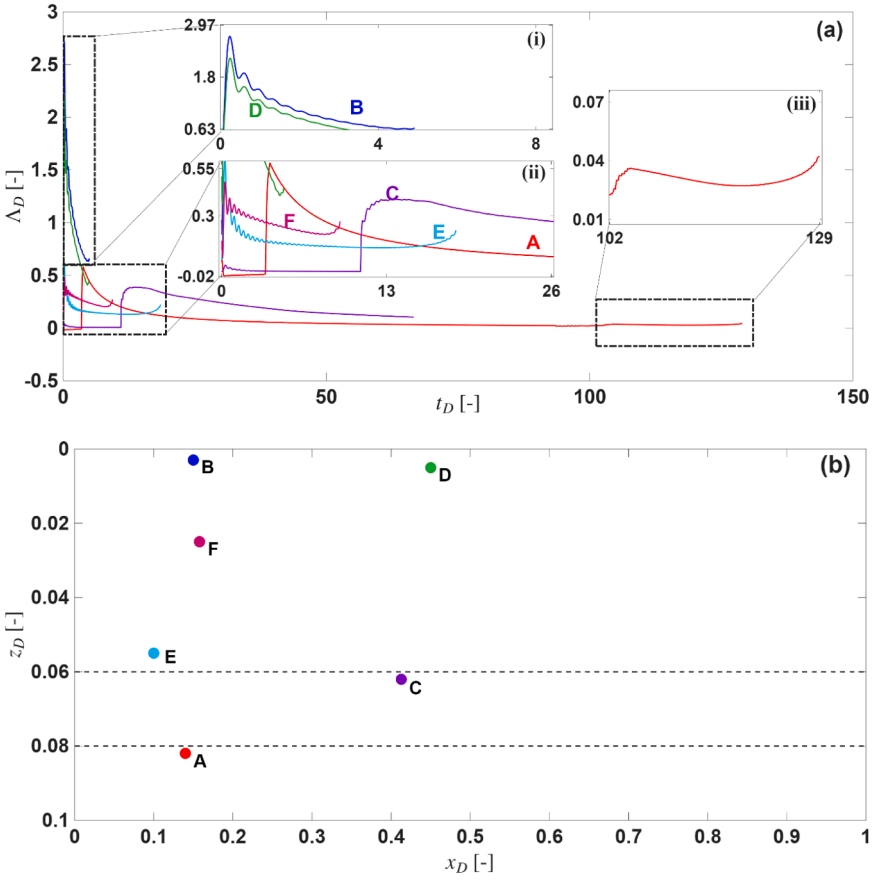

Fig. 13. (a) Temporal evolution of forward FTLE values for particles released at selected locations. Insets emphasize intervals of rapid variation and peak FTLE responses. (b) Spatial distribution of the corresponding particle release points within the modeled domain.

of two distinct rainy seasons in the East African region, motivating an investigation into flow dynamics under such bimodal climatic forcing. Similarly India Meteorological Department (2022) reported that the south East Asia experience two monsoon i.e. southwest and northeast. To incorporate the influence of a bimodal monsoon pattern in the present analysis, the total period P was divided into two equal phases: the first representing the early monsoon event and the second corresponding to the subsequent rainfall episode. For simplicity, both events were assumed to have identical intensity, although Nicholson et al. (2013, 2018) reported that the first event generally corresponds to a longer rainy season, while the second represents a shorter one.

Fig. 12 illustrates particle-tracking simulations performed under both single- and dual-monsoon scenarios by releasing particles at four locations along the top boundary, namely x_D= 0.157, 0.45, 0.74, and 0.997. The flow pattern undergoes marked alteration under the bimodal monsoon condition compared to the single monsoon case, particularly in the local flow regime. The zoomed panels reveal that particle trajectories during the dual monsoon period exhibit more frequent oscillations with shorter wavelengths due to increases fluency of water table peaks in bimodal monsoon scenario. This increased curliness reflects enhanced temporal variability in the hydraulic gradient caused by the repeated attainment of maximum and minimum water table elevations. Furthermore, within the local flow regime, pathlines under the bimodal monsoon penetrate deeper into the aquifer than those under a single monsoon, consistent with the more frequent peaks in the velocity field under bimodal forcing.

3.2.7. *Flow separation and FTLE Analysis*

The deformation of fluid elements in the regional aquifer is governed by the periodic forcing introduced by seasonal water-table fluctuations. The FTLE is employed to quantify the progressive stretching and separation of fluid elements, which may eventually lead to chaotic flow behavior. The FTLE represents the temporal rate of divergence between two fluid particles initially separated by a finite perturbation distance. The mathematical formulation for FTLE evaluation is presented in Sub-section 2.9. The dimensionless FTLE can be represented as $\Lambda_D = \left(\frac{S_{sr1}L^2}{K_{z0}}\right)\Lambda$.

Fluid particles were released from six representative locations, A (0.1400, 0.0805), B(0.1500, 0.0005), C(0.4125, 0.0605), D(0.4500, 0.0050), E(0.1000, 0.0550), and F(0.1580, 0.0250), with an initial dimensionless perturbation length of 0.00005 applied along both x_D and z_D directions. For clarity, these particle release locations are illustrated in Fig. 13(b). The selected particle positions span all three aquifer layers, ensuring a comprehensive representation of the system's hydrogeologic characteristics. Particles A, C, and E are positioned near layer interfaces to capture inter-layer exchange zones where hydraulic contrasts strongly influence particle deformation. Particles B and D are located close to the upper boundary to represent the dominant influence of the periodically varying water-table. Particle F lies within a flow-separation region to examine the sensitivity of particle pathways to local divergence and convergence zones.

Fig. 13(a) presents the temporal evolution of FTLE, depicting the rate of fluid element stretching as the water table oscillates, thereby reflecting the onset of chaotic flow characteristics. Particle A, initiated from the bottom layer, exhibits FTLE values near zero, signifying minimal deformation. This behavior results from the dampening of boundary head fluctuations during their downward propagation, caused by the layered structure and depth-dependent reduction in hydraulic conductivity and specific storage; indicating that flow in the deeper region remains relatively stable. As the particle migrates upward into the middle layer, characterized by lower hydraulic conductivity and higher specific storage, non-uniform head variations emerge, producing a distinct spike in FTLE. However, the low conductivity limits overall particle separation and stretching. Over time, FTLE values gradually decline, partly due to the increasing denominator term in the FTLE formulation and partly owing to the stabilization of particle deformation as the flow field becomes less variable. A small kink is observed around $t_D = 100$, corresponding to the particle's transition into the upper layer, though the associated FTLE magnitude remains low and transient. A similar trend is observed for particle C, which exhibits a sharp increase in FTLE upon entering the upper layer, followed by a gradual decrease. In contrast, particles B, D, E, and F show consistently higher FTLE values, indicating stronger particle stretching and deformation near the upper boundary of the aquifer, where the influence of water table fluctuations is most pronounced compared to the deeper zones.

Most groundwater flow models assume homogeneous aquifer properties and neglect vertical variability in hydraulic parameters, potentially underestimating the system's intrinsic chaotic behavior. To address this, FTLE analysis was conducted under two contrasting hydraulic configurations: (i) depth-decaying hydraulic parameters and (ii) equivalent homogeneous parameterization. The definitions of the heterogeneous and equivalent homogeneous configurations are identical to those described in Sub-section 3.2.3.

Fig. 14 compares particle dynamics under these two aquifer representations. In both scenarios, particles were released from the same initial locations, with particles B, D, E and F selected for detailed analysis, as the middle and bottom layers contribute less to the manifestation of natural chaotic behavior compared to the upper layer. The results demonstrate that particle separation is substantially greater in the depth-decaying aquifer than in the equivalent homogeneous aquifer. Chaotic advection is primarily driven by periodic water-table

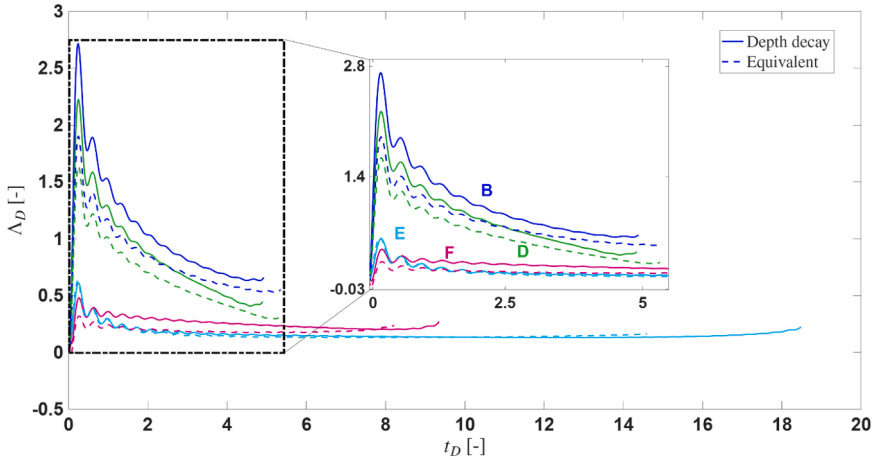

Fig. 14. Comparison of FTLEs for aquifers characterized by depth-decaying and equivalent homogeneous hydraulic parameters.

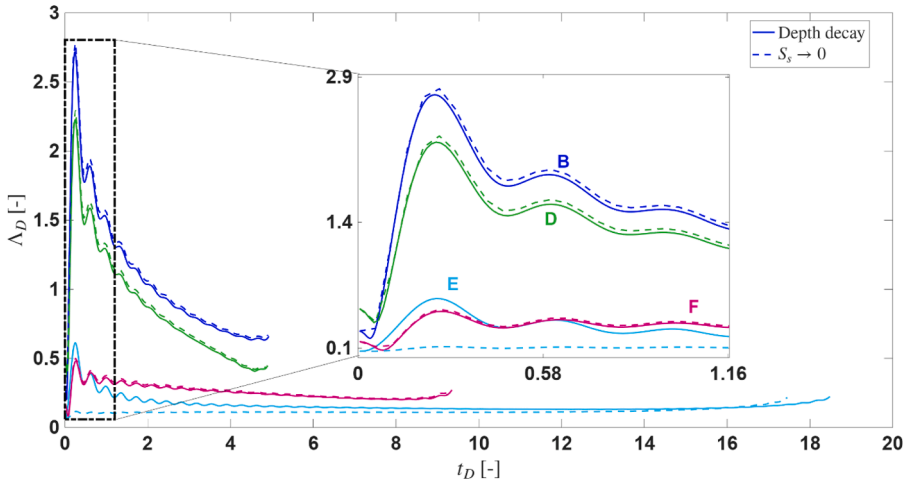

Fig. 15. Comparison of FTLEs for aquifer systems simulated with (solid line) and without (dashed line) specific storage effects.

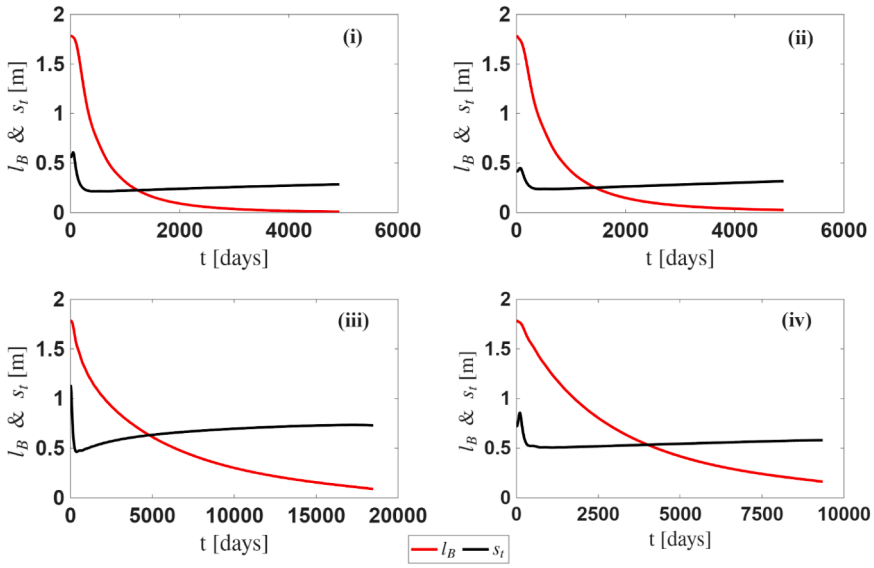

Fig. 16. Stretching length s_t (red) and diffusion scale l_B (black) for particles (i) B, (ii) D, (iii) E, and (iv) F. The crossover times ($s_t = l_B$) occur at around 1230, 1445, 4760, and 3980 days, respectively.

fluctuations at the upper boundary, and the higher near-surface conductivities in depth-decaying aquifers enhance vertical velocity gradients, promoting stronger stretching and folding of particle trajectories. This results in more pronounced chaotic dynamics compared to the equivalent depth-averaged aquifer. Notably, if a homogeneous aquifer is assigned a uniformly high conductivity equal to the maximum near-surface value of the depth-decaying profile, the resulting chaotic behavior can approach that of the depth-decaying aquifer.

Further analysis was performed to examine the role of aquifer specific storage in governing flow separation and the emergence of chaotic fluid-particle motion. Fig. 15 presents the FTLE results comparing two configurations: aquifers with finite specific storage, and aquifers without storage effects, represented by a quasi-steady-state condition. As discussed earlier, flow separation predominantly occurs for fluid particles originating from the upper layer; hence, the present analysis focuses on particles released from points B, D, E, and F.

The results indicate that under quasi-steady-state conditions, the FTLE values associated with particles released from the upper layer are marginally higher than those in the case considering specific storage. This behavior arises because instantaneous head variations induced by water-table oscillations, when specific storage is neglected, generate a slightly more chaotic flow response compared to aquifers with storage effects. This finding underscores the moderating influence of specific storage on the transmission of water-table fluctuations through the aquifer.

To further assess the extent of chaotic advection in regional aquifers, an analysis is carried out to determine whether mixing in the aquifer is controlled primarily by chaotic stretching or by molecular diffusion. This is achieved by evaluating two characteristic length scales over time: the Batchelor (diffusive) scale and the stretching thickness. The Batchelor scale is defined as $l_B = \sqrt{\frac{D_m}{\gamma}}$, where D_m is the molecular diffusion coefficient in groundwater (10^{-9} m^2/s), and γ is the time-averaged compression rate, approximated by the time-averaged FTLE (Batchelor, 1959; Brett et al., 2019; Götzfried et al., 2019). The Batchelor scale represents the equilibrium between diffusive broadening and advective thinning of fluid filaments.

The evolution of the stretching thickness is described by $s_t = s_0 \exp(-\gamma t)$, where s_0 is the initial filament thickness (Götzfried et al., 2019; Meunier and Villermaux, 2010). Chaotic advection elongates fluid elements along the stretching direction while compressing them in the transverse direction, leading to progressive filament thinning until

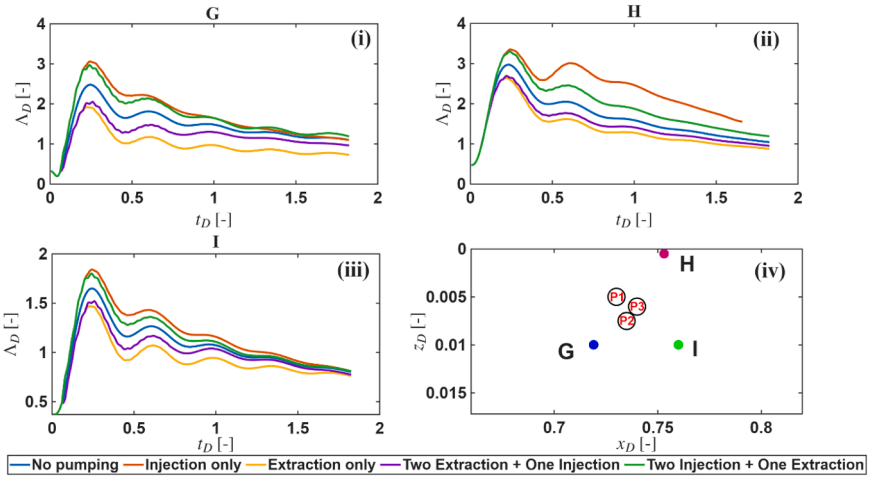

Fig. 17. (i–iii) FTLE evolution for particles G, H, and I under five pumping configurations. (iv) Pump and particle release locations, where P1, P2, and P3 denote the pump positions and G, H, and I denote the particle positions.

diffusion becomes dominant. The initial filament thickness s_0 is estimated from the local characteristic deformation length $l_s = \frac{V_R}{|dV_R/dz|}$, where V_R is the resultant groundwater velocity. This scale quantifies the distance over which velocity varies significantly due to vertical shear and represents the initial lamella size prior to deformation (Ottino, 1989). The characteristic length was evaluated at the midpoint of the first layer at $t = 0.50P$, corresponding to the maximum water-table elevation. Although previous studies have adopted $s_0 \approx l_s$, the kilometer-scale domain considered here yields unrealistically large initial filament thicknesses. Therefore, we adopt $s_0 \approx 0.05l_s$, resulting in an initial thickness of approximately 1.75 m, which is more representative of subsurface mixing scales while preserving proportionality to local shear intensity.

Fig. 16 shows the temporal evolution of s_t and l_B for particles B, D, E, and F. The crossover time, when $s_t \approx l_B$, indicates the transition from advection-dominated to diffusion-dominated mixing, occurring at approximately 1230 days, 1445 days, 4760 days, and 3980 days, for initial release points B, D, E and F, respectively. Prior to these times, chaotic advection dominates mixing, indicating that sustained stretching induced by periodic water-table fluctuations can significantly enhance solute dilution.

To evaluate whether chaotic advection substantially enhances mixing compared to pure diffusion, we estimated the purely diffusive mixing timescale over a characteristic filament length $l_s \sim s_0 \approx 1.75$ m as $t_{\text{diff}} = \frac{{l_s}^2}{D_m} \approx 3.5 \times 10^4$ days which is orders of magnitude larger than the crossover times observed in the aquifer. This demonstrates that stretching induced by chaotic advection accelerates mixing significantly before molecular diffusion dominates.

The temporal evolution of s_t shows an initial rapid decline for all particles, indicating strong early-time deformation, followed by slower decay. The diffusion scale l_B increases gradually as the FTLE diminishes over time. The results further reveal strong spatial variability in mixing efficiency. Particles E and F remain in the advection-dominated regime for much longer durations, indicating zones of persistent velocity gradients and enhanced mixing potential, whereas particles B and D transition earlier to diffusion-dominated behavior. These differences highlight the heterogeneous nature of mixing in regional aquifers and suggest that chaotic advection can be highly localized. The Péclet number is evaluated as $P_e = \frac{\gamma {l_s}^2}{D_m}$, and corresponding Péclet number for these particles are on the order of $10^3 - 10^4$, consistent with advection-dominated transport in groundwater systems (Ghanbarian et al., 2023).

3.2.8. *Design of engineered extraction/injection to increase the chaotic advection*

Chaotic advection under natural water-table fluctuations demonstrated that transient hydrodynamics alone can induce stretching and mixing within the upper aquifer. Building on this behavior, the present analysis investigates whether chaotic advection can be deliberately enhanced through engineered pumping strategies to improve subsurface mixing and potentially increase groundwater remediation efficiency.

Three pumping wells were installed at locations (0.730, 0.0050), (0.740, 0.0075), and (0.7350, 0.0060), denoted as P1, P2, and P3, respectively in Fig. 17(iv). These staggered positions were intentionally selected to break spatial symmetry and promote stronger deformation of flow paths. Four pumping configurations were examined: (a) injection only in all three wells, (b) extraction only from all three wells, (c) two injection wells combined with one extraction well, and (d) one injection well combined with two extraction wells. All configurations were evaluated relative to a natural (no-pumping) reference case.

To introduce temporal variability, a cyclic pulsed-pumping strategy was implemented, consisting of 20-day ON and 20-day OFF cycles. Pumping pulses were initiated every 40 days, with phase-shifted start times of 60, 140, and 200 days for the three wells, generating distinct pumping histories over a two-year simulation period. This staggered activation produces sustained temporal heterogeneity in the flow field, promoting repeated stretching and folding of fluid elements and thereby enabling an engineered mechanism for inducing chaotic advection.

Particles were released at locations (0.7190, 0.0100), (0.7530, 0.0005), and (0.7600, 0.0100) named as G, H, and I, respectively in Fig. 17(iv), and the evolution of the FTLE was evaluated for each pumping configuration. As shown in Fig. 17(i-iii), the injection-only configuration consistently produces the highest FTLE values, particularly at early times. Injection generates localized hydraulic head mounds that oppose the natural downward flow direction, periodically inducing flow reversals over the 40-day pumping cycle. These alternating flow directions significantly enhance particle stretching and chaotic deformation. In contrast, extraction-only pumping yields the lowest FTLE values, in several cases falling below those observed under natural conditions. Although extraction increases local flow velocities, it creates a convergent sink that draws streamlines smoothly toward the well, thereby suppressing flow deformation and reducing chaotic stretching.

The configuration with two injection wells and one extraction well exhibits strong initial stretching due to pronounced flow asymmetry; however, FTLE values decay rapidly as particles migrate away from the high-gradient regions near the injection wells. Similarly, the configuration with two extraction wells and one injection well shows weaker chaotic stretching than the natural case, as extraction dominates the

local flow field and suppresses the deformation generated by water-table fluctuations.

Overall, these results indicate that injection-driven perturbations are the most effective mechanism for generating sustained chaotic advection when superimposed on naturally fluctuating water-table conditions in a nested flow system. In contrast, extraction tends to suppress chaotic deformation despite increasing local flow velocities. This distinction highlights the potential for engineered injection strategies to be used as a tool for enhancing mixing and transport efficiency in managed aquifer recharge and in-situ remediation applications.

3.2.9. Model limitations and future scope

Although the present study advances analytical regional groundwater flow modeling and enhance its physical realism, it still has certain limitations, which are noted below.

i. The model assumes a deterministic, depth-dependent decline in hydraulic parameters but does not capture their stochastic spatial variability, which is common in natural aquifer systems.
ii. The model has not been calibrated or validated against laboratory-scale sand tank experiments or site-specific field observations. In regional-scale settings, field validation is particularly challenging because:

- Limited spatiotemporal head observations: Validation of transient flow dynamics requires long-term water-level monitoring from nested piezometer clusters distributed across the basin. Such dense, depth-resolved datasets are rarely available in regional aquifers.
- Difficulty in obtaining depth-dependent hydraulic parameters: Reliable estimates of vertical hydraulic conductivity and specific storage at multiple depths require multi-depth pumping or cross-hole tests. These tests are logistically demanding in thick alluvial formations and typically provide vertically averaged values, necessitating additional drilling or geophysical methods to resolve vertical variability.
- Complexity of representing the top boundary in real systems: The analytical model assumes a smoothly undulating water table influenced by uniformly spaced streams. In reality, water-table configurations are shaped by complex surface topography, irregular stream networks, heterogeneous water-body distribution, and varying perennial/ephemeral behavior. Validating such a boundary would require continuous and spatially distributed water-table measurements across the basin, data that are generally unavailable at regional scales.

iii. The model requires knowledge of hydraulic conductivity and specific storage at the top of each layer. While high-resolution tools such as direct-push permeameters, electrical resistivity imaging, and borehole NMR can improve parameter estimation, obtaining reliable layer-top values typically requires deep coring and laboratory testing. Future work should integrate these advanced characterization methods to better constrain layer-specific properties for analytical model applications.
iv. The unsaturated zone, which significantly influences recharge and vadose–saturated flow coupling, is not represented in the current formulation.

In addition, the present study employs an exponential decay formulation for depth-dependent hydraulic conductivity, which offers a coupled representation of $K(z)$ and $\theta(z)$ necessary for flow-line and travel-time analysis. However, alternative empirical formulations such as the integrated permeability-depth model proposed by Kuang and Jiao (2014) may be more suitable in geological settings where field observations indicate a stronger power-law dependence with depth. Although adopting such models would require re-derivation of the analytical solution (through modified filter functions), their incorporation represents an important direction for expanding the model's applicability to diverse hydro-stratigraphic environments.

Future work should focus on coupling the present flow framework with solute transport models to better quantify contaminant migration, stretching-enhanced mixing, and dispersion under both natural and anthropogenic stresses. Extensions to fully three-dimensional, transient formulations and integration of dynamically varying surface-water bodies would further improve the model's capability to capture basin-scale groundwater flow and surface–subsurface interactions.

4. Conclusion

In this study, a two-dimensional analytical model was developed for a multilayer regional aquifer system incorporating depth-decaying hydraulic conductivity and specific storage, subjected to temporally fluctuating water table boundary and periodic pumping. The model was derived using the GITT, ensuring implicit continuity of head and flux across layer interfaces without requiring iterative eigenvalue estimation. Model performance was verified against a previously established single-layer analytical solution and further evaluated through comparison with COMSOL-based numerical simulations. Although the analytical solution involves nested matrices and series, it provides key advantages over numerical methods. Once the eigenfunctions and coefficients are computed, hydraulic heads and fluxes can be evaluated at any location and time without mesh refinement or iterative time stepping. The solution preserves exact continuity across layers, avoids numerical dispersion, and enables precise evaluation of hydrologically important features, such as stagnation points, while offering clear physical insight into parameter sensitivity and boundary forcing. These features highlight the practical efficiency and continued relevance of the proposed analytical framework for groundwater studies.

The key findings of this study are summarized as follows:

(i) Sensitivity analysis identified the vertical hydraulic conductivity of the upper and middle aquifers, the depth-decay coefficient of the upper layer, the specific storage of the middle layer, and the pumping rate as the most influential parameters governing the hydraulic head response.
(ii) Uncertainty analysis demonstrated that variations in specific storage and hydraulic conductivity substantially affect head evolution over time, with the middle aquifer amplifying head prediction uncertainty due to its relatively higher storage capacity.
(iii) The recharge/discharge distribution, evaluated under depth-decaying, equivalent homogeneous and pumping scenarios, revealed that equivalent parameterization tends to underestimate recharge/discharge magnitudes. Pumping enhanced recharge near the extraction zone, reflecting strong local-scale perturbations to regional flow balance.
(iv) The analysis of particle flow dynamics underscored the critical influence of aquifer specific storage on transient flow behavior under fluctuating water table conditions. Storage effects introduce temporal lag and spatially asynchronous head responses, giving rise to spiral and oscillatory pathlines near pseudo-stagnation zones where particles exhibit prolonged residence times.
(v) Under pumping conditions, the natural bifurcation and oscillatory motion of flowlines are markedly suppressed. Continuous extraction shifts the position of stagnation zones and generates predominantly unidirectional flow patterns, thereby attenuating the intrinsic dynamism of the groundwater system.
(vi) The FTLE analyses illustrated that transient boundary forcing induces chaotic advection in the aquifer system Chaotic advection is further enhanced under intermittent injection with shorter time periods, highlighting its potential application in in-situ aquifer remediation.

Overall, the developed analytical framework provides an efficient and physically interpretable approach for examining transient regional flow processes in vertically heterogeneous aquifers. It also offers a benchmark for testing and validating numerical models and for exploring the onset of chaotic flow behavior in natural groundwater systems.

Declaration of generative AI and AI-assisted technologies in the manuscript preparation process

During the preparation of this work the authors used ChatGPT in order to improve language and readability of the manuscript. After using this tool, the authors reviewed and edited the content as needed and take full responsibility for the content of the published article.

CRediT authorship contribution statement

Saurabh Maurya: Writing – original draft, Validation, Software, Methodology, Formal analysis, Conceptualization. **Ratan Sarmah:** Writing – review & editing, Visualization, Supervision, Methodology, Conceptualization. **Ickkshaanshu Sonkar:** Writing – review & editing, Supervision, Methodology.

Declaration of competing interest

The authors declare that they have no known competing financial interests or personal relationships that could have appeared to influence the work reported in this paper.

Acknowledgements

The authors acknowledge the Indian Institute of Technology Ropar (IIT Ropar) for facilitating this research.

Supplementary materials

Supplementary material associated with this article can be found, in the online version, at doi:10.1016/j.advwatres.2026.105215.

Appendix A: Derivation of the Analytical Form of $V_i(r_D, t_D)$ from Eq. (27)

The analytical expression for $V_i(\mathbf{r}_D, t_D)$ is derived by solving Eq. (27) subject to the interface and boundary conditions specified in Eqs. (28)-(33), using the separation of variables approach. Incorporating the dimensionless depth-dependent hydraulic conductivity defined in Eq. (17) into the governing equation for V_i (Eq. (27) leads to:

$$\left(\frac{K_{xB_{i-1}^+}}{K_{z0}}\right)\frac{\partial^2 V_i}{\partial^2 x_D}+\left(\frac{K_{zB_{i-1}^+}}{K_{z0}}\right)\left(\frac{\partial^2 V_i}{\partial^2 z_D}-A_{Di}\frac{\partial V_i}{\partial z_D}\right)=0,\quad \mathbf{r}_D\in\Omega_{Di} \tag{A1}$$

Eq. (A1) is solved using the separation of variables approach (Haberman, 2013), assuming V_i can be written as the product of two independent functions of x_D and z_D, i.e., $V_i = X(x_D)Z_i(z_D)$. Substituting this into Eq. (A1) yields:

$$\frac{X''(x_D)}{X(x_D)}=-\left(\frac{K_{zB_{i-1}^+}}{K_{xB_{i-1}^+}}\right)\left[\frac{Z_i''(z_D)}{Z_i(z_D)}-A_{Di}\frac{Z_i'(z_D)}{Z_i(z_D)}\right]=-\lambda^2, \tag{A2}$$

where λ^2 is a positive separation constant. The function of x_D is then governed by:

$$X''(x_D)+\lambda^2 X(x_D)=0. \tag{A3}$$

The general solution of Eq. (A3) is:

$$X(x_D)=R\cos(\lambda x_D)+S\sin(\lambda x_D), \tag{A4}$$

where R and S are arbitrary constants. By applying the boundary conditions given in Eqs. (28) and (29), Eq. (A4) reduces to:

$$X(x_D)=R_k\cos(k\pi x_D),\ k=0,\ 1,\ 2,\ 3.... \tag{A5}$$

where $\lambda = k\pi$. It is important to note that the function V_i is solved subject to the boundary conditions defined in Eqs. (28)-(33), among which Eq. (33) prescribes a transient water-table condition. Consequently, in the subsequent derivation, the coefficient R_k is treated as a function of t_D, thereby incorporating the time-dependent boundary into the analytical framework.

Equating the middle term of Eq. (A2) to the separation constant $-\lambda^2$ gives:

$$Z_i''(z_D)-A_{Di}Z_i'(z_D)-\left(\frac{K_{xB_{i-1}^+}}{K_{zB_{i-1}^+}}\right)\lambda^2 Z_i(z_D)=0. \tag{A6}$$

The general solution of Eq. (A6) can be expressed in hyperbolic form as:

$$Z_i(z_D)=\exp\left(\frac{A_{Di}}{2}z_D\right)[C_{ki}\cosh(\gamma_{ki}z_D)+D_{ki}\sinh(\gamma_{ki}z_D)], \tag{A7}$$

where

$$\gamma_{ki} = \sqrt{\left(\frac{A_{Di}}{2}\right)^2 + \left(\frac{K_{xB_{i-1}^+}}{K_{zB_{i-1}^+}}\right)(k\pi)^2}. \tag{A8}$$

Finally, combining Eqs. (A5) and (A7) and applying the principle of superposition for linear differential equations (Haberman, 2013), the solution for V within the i^{th} layer is written as:

$$V_i(\boldsymbol{r}_D,\ t_D) = \exp\left(\frac{A_{Di}}{2}z_D\right)\sum_{k=0}^{\infty} R_k(t_D)\cos(k\pi x_D)[C_{ki}\cosh(\gamma_{ki}z_D) + D_{ki}\sinh(\gamma_{ki}z_D)]. \tag{A9}$$

The next step is to determine the unknown coefficients R_k, in Eq. (A9). Applying the water-table boundary condition [Eq. (33)] gives:

$$V_1(x_D,\ 0,\ t_D) = h_{DWT}(x_D,\ t_D) = \sum_{k=0}^{\infty} R_k(t_D)\cos(k\pi x_D)C_{k1}. \tag{A10}$$

To simplify the representation, we choose C_{k1} equal to 1, allowing $R_k(t_D)$ to represent the temporal dependence of water-table fluctuations directly. Thus:

$$C_{k1} = 1, \tag{A11}$$

and

$$h_{DWT}(x_D,\ t_D) = \sum_{k=0}^{\infty} R_k(t_D)\cos(k\pi x_D). \tag{A12}$$

Substituting the water-table expression from Eq. (33) and applying a Fourier cosine series expansion over the range $0 < x_D < 1$, the coefficients $R_k(t_D)$ can be obtained as:

$$R_k(t_D) = \begin{cases} 1 + \varepsilon\left(\frac{H_L}{H_R}\right)\sin^2(\omega t_D) & k = 0 \\ -1 & k = 1 \\ -\varepsilon\left(\frac{H_L}{H_R}\right)\sin^2(\omega t_D) & k = f \\ 0 & k \notin \{0,\ 1,\ \mathrm{f}\} \end{cases}. \tag{A13}$$

For getting the coefficients C_{ki} and D_{ki} it is needed to apply interface and boundary conditions, Eqs. (31)-(32) to Eq. (A9).

Applying the head continuity condition between two adjacent layers i and i+1, as defined in Eq. (31), to Eq. (A9) and carrying out a Fourier expansion along $0 < x_D < 1$ leads to the following interfacial relation:

$$\exp\left[(A_{Di} - A_{D(i+1)})\frac{B_{Di}}{2}\right][C_{ki}\cosh(\gamma_{ki}B_{Di}) + D_{ki}\sinh(\gamma_{ki}B_{Di})] = [C_{k(i+1)}\cosh(\gamma_{k(i+1)}B_{Di}) + D_{k(i+1)}\sinh(\gamma_{k(i+1)}B_{Di})]. \tag{A14}$$

Next, by applying the flux continuity condition between the adjacent layers, as given in Eq. (32), to Eq. (A9) and carrying out the Fourier expansion along the same domain ($0 < x_D < 1$), one obtains:

$$\begin{aligned} &K_{zDi}(B_{Di})\exp\left(\frac{A_{Di}}{2}B_{Di}\right)\left\{\gamma_{ki}[C_{ki}\sinh(\gamma_{ki}B_{Di}) + D_{ki}\cosh(\gamma_{ki}B_{Di})] + \left(\frac{A_{Di}}{2}\right)[C_{ki}\cosh(\gamma_{ki}B_{Di}) + D_{ki}\sinh(\gamma_{ki}B_{Di})]\right\} \\ &= K_{zD(i+1)}(B_{Di})\exp\left(\frac{A_{D(i+1)}}{2}B_{Di}\right)\left\{\gamma_{k(i+1)}[C_{k(i+1)}\sinh(\gamma_{ki}B_{Di}) + D_{k(i+1)}\cosh(\gamma_{ki}B_{Di})] + \left(\frac{A_{D(i+1)}}{2}\right)[C_{k(i+1)}\cosh(\gamma_{k(i+1)}B_{Di}) + D_{k(i+1)}\sinh(\gamma_{k(i+1)}B_{Di})]\right\}. \end{aligned} \tag{A15}$$

Lastly, applying the no-flow boundary condition at the base of the bottom layer, as defined in Eq. (30), to Eq. (A9) and performing a Fourier expansion over the domain $0 < x_D < 1$, yields the following relation:

$$[C_{k3}\sinh(\gamma_{k3}B_D) + D_{k3}\cosh(\gamma_{k3}B_D)] + \left(\frac{A_{D3}}{2\gamma_{k3}}\right)[C_{k3}\cosh(\gamma_{k3}B_D) + D_{k3}\sinh(\gamma_{k3}B_D)] = 0. \tag{A16}$$

For a three-layer aquifer system, there are six unknowns (C_{ki},D_{ki}), while $R_k(t_D)$ has already been determined from Eq. (A13). These coefficients are determined simultaneously from Eqs. (A11) and (A14)–(A16) for each k using Cramer's rule or another appropriate matrix-solving technique (Piskunov, 1969). Substituting the evaluated coefficients along with $R_k(t_D)$ into Eq. (A9) yields the complete analytical solution for $V_i(\boldsymbol{r}_D,\ t_D)$.

Appendix B: Derivation of the Analytical Form of $U(\boldsymbol{r}_D,\ t_D)$ from Eq. (47)

The analytical expression for $U(\boldsymbol{r}_D,\ t_D)$ is derived by solving Eq. (47) under the boundary conditions specified in Eqs. (37)-(40) and (43), employing the GITT (Cotta, 2020; Deng et al., 2014; Mikhailov and Ozisik, 1983). To address this boundary value problem, a two-dimensional generalized integral transform pair is formulated by selecting appropriate Eigen-functions associated with auxiliary Sturm–Liouville problems along the x_D-and z_D-directions:

$$\nabla^2_{x_D}\varphi_m(x_D) + (M_m)^2\varphi_m(x_D) = 0, \tag{B1}$$

$$\nabla^2_{z_D}\Psi_n(z_D) + (N_n)^2\Psi_n(z_D) = 0, \tag{B2}$$

where φ_m and Ψ_n represent the eigenfunctions of the auxiliary problems defined in Eqs. (B1) and (B2), respectively. Eq. (B1) is solved subject to the homogeneous Neumann boundary conditions $\frac{d\varphi_m}{dx_D} = 0$ at $x_D = 0,\ 1$; consistent with the representative boundary conditions in Eqs. (38) and (39). Similarly, Eq. (B2) is solved considering $\Psi_n(0) = 0$ and $\frac{d\Psi_n}{dz_D} = 0$ at $z_D = 0,\ B_D$ respectively, in accordance with the representative boundary conditions in Eqs. (40) and (43). The corresponding analytical expressions for the eigenfunctions are obtained as:

$$\varphi_m(x_D) = \cos(M_m x_D),\ m = 0,\ 1,\ 2,\ 3\cdots \tag{B3}$$

$$\Psi_n(z_D) = \sin(N_n z_D),\ n = 1,\ 2,\ 3\cdots \tag{B4}$$

with eigenvalues defined by $M_m = m\pi$ and $N_n = \left(\frac{1-2n}{2}\right)\frac{\pi}{B_D}$.

The eigenfunctions φ_m and Ψ_n of the Sturm-Liouville problems satisfy the orthonormal condition (Haberman, 2013), expressed as:

$$\frac{1}{\sqrt{\alpha_m}\sqrt{\alpha_p}}\int_0^1 \varphi_m(x_D)\varphi_p(x_D)dx_D = \delta_m^p, \tag{B5}$$

$$\frac{1}{\sqrt{\beta_n}\sqrt{\beta_q}}\int_0^{B_D} \Psi_n(z_D)\Psi_q(z_D)dz_D = \delta_n^q, \tag{B6}$$

where δ_m^p denotes the Kronecker delta, equal to 1 when $m = p$ and 0 otherwise. The normalization coefficients are given by:

$$\alpha_m = \int_0^1 [\varphi_m(x_D)]^2 dx_D, \tag{B7}$$

$$\beta_n = \int_0^{B_D} [\Psi_n(z_D)]^2 dz_D, \tag{B8}$$

Here, p and q serve as dummy indices for m and n, respectively.

Using the orthogonality property of the eigenfunctions, the forward generalized integral transform is ansatz in the form:

$$T_{mn}(t_D) = \frac{1}{\sqrt{\alpha_m\beta_n}}\int_0^1\int_0^{B_D} U(x_D,\ z_D,\ t_D)\varphi_m(x_D)\Psi_n(z_D)dx_D dz_D, \tag{B9}$$

and the inverse relation reconstructs the solution as:

$$U(x_D,\ z_D,\ t_D) = \sum_{m=0}^{\infty}\sum_{n=1}^{\infty} T_{mn}(t_D)\frac{\varphi_m(x_D)\Psi_n(z_D)}{\sqrt{\alpha_m\beta_n}}. \tag{B10}$$

The coefficient $T_{mn}(t_D)$ are determined by applying the transform operator $\frac{1}{\sqrt{\alpha_m\beta_n}}\int_0^1\int_0^{B_D}(\cdot)\varphi_m(x_D)\Psi_n(z_D)dx_D dz_D$ to Eq. (47), yields:

$$\begin{aligned}
&\frac{1}{\sqrt{\alpha_m\beta_n}}\int_0^1\int_0^{B_D} S_{sD}(z_D)\frac{\partial U}{\partial t_D}\varphi_m(x_D)\Psi_n(z_D)dx_D dz_D + \frac{1}{\sqrt{\alpha_m\beta_n}}\int_0^1\int_0^{B_D}\left\{-\frac{\partial}{\partial x_D}\left[K_{xD}(z_D)\frac{\partial U}{\partial x_D}\right]\right\}\varphi_m(x_D)\Psi_n(z_D)dx_D dz_D + \frac{1}{\sqrt{\alpha_m\beta_n}}\int_0^1\int_0^{B_D}\Bigg\{\\
&-\frac{\partial}{\partial z_D}\left[K_{zD}(z_D)\frac{\partial U}{\partial z_D}\right]\Bigg\}\varphi_m(x_D)\Psi_n(z_D)dx_D dz_D\\
&= -\frac{1}{\sqrt{\alpha_m\beta_n}}\int_0^1\int_0^{B_D} S_{sD}(z_D)\frac{\partial V}{\partial t_D}\varphi_m(x_D)\Psi_n(z_D)dx_D dz_D - \frac{1}{\sqrt{\alpha_m\beta_n}}\int_0^1\int_0^{B_D}[\,Q_D(t_D)\delta(x_D - x_{D0})\delta(z_D - z_{D0})]\varphi_m(x_D)\Psi_n(z_D)dx_D dz_D.
\end{aligned} \tag{B11}$$

By substituting the expression for $U(x_D,\ z_D,\ t_D)$ from Eq. (B10) into Eq. (B11), replacing the indices (m, n) with dummy indices (p, q), and rearranging the resulting terms, a system of coupled ordinary differential equations (ODEs) is obtained:

$$\sum_{p=0}^{\infty}\sum_{q=1}^{\infty} E_{pq}^{mn}\frac{dT_{pq}(t_D)}{dt_D} + \sum_{p=0}^{\infty}\sum_{q=1}^{\infty} F_{pq}^{mn}T_{pq}(t_D) = G^{mn}(t_D). \tag{B12}$$

The first term in Eq. (B12) originates from the first term of Eq. (B11), and the formation of subsequent terms follows analogously. Specifically, substituting Eq. (B10) into the first term of Eq. (B11) gives:

$$\sum_{p=0}^{\infty}\sum_{q=1}^{\infty} E_{pq}^{mn}\frac{dT_{pq}(t_D)}{dt_D} = \frac{1}{\sqrt{\alpha_m\beta_n}}\int_0^1\int_0^{B_D} S_{sD}(z_D)\frac{\partial U}{\partial t_D}\varphi_m(x_D)\Psi_n(z_D)dx_D dz_D = \frac{1}{\sqrt{\alpha_m\beta_n}}\int_0^1\int_0^{B_D} S_{sD}(z_D)\frac{\partial}{\partial t_D}\left[\sum_{p=0}^{\infty}\sum_{q=1}^{\infty} T_{pq}(t_D)\frac{\varphi_p(x_D)\Psi_q(z_D)}{\sqrt{\alpha_p\beta_q}}\right]\varphi_m(x_D)\Psi_n(z_D)dx_D dz_D. \tag{B13}$$

By interchanging the order of summation and differentiation, Eq. (B13) simplifies to:

$$\sum_{p=0}^{\infty}\sum_{q=1}^{\infty}E_{pq}^{mn}\frac{dT_{pq}(t_D)}{dt_D}=\sum_{p=0}^{\infty}\sum_{q=1}^{\infty}\frac{dT_{pq}}{dt_D}\int_0^1\frac{\varphi_p(x_D)\varphi_m(x_D)}{\sqrt{\alpha_p\alpha_m}}dx_D\int_0^{B_D}S_{sD}(z_D)\frac{\Psi_n(z_D)\Psi_q(z_D)}{\sqrt{\beta_n\beta_q}}dz_D. \tag{B14}$$

By equating the coefficients of $\frac{dT_{pq}(t_D)}{dt_D}$ on both sides of Eq. (B14), the matrix element E_{pq}^{mn} is obtained as:

$$E_{pq}^{mn}=\int_0^1\frac{\varphi_p(x_D)\varphi_m(x_D)}{\sqrt{\alpha_p\alpha_m}}dx_D\int_0^{B_D}S_{sD}(z_D)\frac{\Psi_n(z_D)\Psi_q(z_D)}{\sqrt{\beta_n\beta_q}}dz_D. \tag{B15}$$

Using the orthogonality relation (Eq. B5) and the layered definition of $S_{sD}(z_D)$ from Eq. (44), Eq. (B15) reduces to:

$$E_{pq}^{mn}=\delta_m^p\sum_{i=1}^{3}\int_{B_{D(i-1)}}^{B_{Di}}S_{sDi}(z_D)\frac{\Psi_n(z_D)\Psi_q(z_D)}{\sqrt{\beta_n\beta_q}}dz_D, \tag{B16}$$

with $B_{D0}=0$ and $B_{D3}=B_D$. Substituting the explicit expressions for Ψ and S_{sDi}, and evaluating the integrals, yields the elements of the coefficient matrix E_{pq}^{mn}.

Next, the equivalence between the second term of Eq. (B12) and the diffusion terms of Eq. (B11) is established. Applying integration by parts to the second and third terms of Eq. (B11) yields:

$$\begin{aligned}\sum_{p=0}^{\infty}\sum_{q=1}^{\infty}F_{pq}^{mn}T_{pq}(t_D)&=\frac{1}{\sqrt{\alpha_m\beta_n}}\int_0^1\int_0^{B_D}\left\{-\frac{\partial}{\partial x_D}\left[K_{xD}(z_D)\frac{\partial U}{\partial x_D}\right]\right\}\varphi_m(x_D)\Psi_n(z_D)dx_Ddz_D+\frac{1}{\sqrt{\alpha_m\beta_n}}\int_0^1\int_0^{B_D}\left\{-\frac{\partial}{\partial z_D}\left[K_{zD}(z_D)\frac{\partial U}{\partial z_D}\right]\right\}\varphi_m(x_D)\Psi_n(z_D)dx_Ddz_D\\&=\frac{-1}{\sqrt{\alpha_m\beta_n}}\int_0^{B_D}K_{xD}(z_D)\left[\int_0^1\frac{\partial^2U}{\partial x_D^2}\varphi_m(x_D)dx_D\right]\Psi_n(z_D)dz_D-\frac{1}{\sqrt{\alpha_m\beta_n}}\int_0^1\left[K_{zD}(z_D)\frac{\partial U}{\partial z_D}\Psi_n(z_D)\Big|_0^{B_D}-\int_0^{B_D}K_{zD}(z_D)\frac{\partial U}{\partial z_D}\frac{d\Psi_n}{dz_D}dz_D\right]\varphi_m(x_D)dx_D.\end{aligned} \tag{B17}$$

Incorporating the expression for U into Eq. (B17), and noting that the boundary term $K_{zD}(z_D)\frac{\partial U}{\partial z_D}\Psi_n(z_D)|_0^{B_D}=0$ (due to the boundary condition along the z_D-direction), the equation reduces to:

$$\sum_{p=0}^{\infty}\sum_{q=1}^{\infty}F_{pq}^{mn}T_{pq}=\frac{-1}{\sqrt{\alpha_m\beta_n}}\int_0^{B_D}K_{xD}(z_D)\left[\sum_{p=0}^{\infty}\sum_{q=1}^{\infty}T_{pq}\int_0^1\frac{d^2\varphi_p}{dx_D^2}\varphi_m(x_D)\Psi_q(z_D)dx_D\right]\Psi_n(z_D)dz_D+\frac{1}{\sqrt{\alpha_m\beta_n}}\int_0^1\left[\sum_{p=0}^{\infty}\sum_{q=1}^{\infty}T_{pq}\int_0^{B_D}K_{zD}(z_D)\frac{d\Psi_q}{dz_D}\frac{d\Psi_n}{dz_D}\varphi_p(x_D)dz_D\right]\varphi_m(x_D)dx_D. \tag{B18}$$

By interchanging the order of summation and differentiation, Eq. (B18) simplifies to:

$$\sum_{p=0}^{\infty}\sum_{q=1}^{\infty}F_{pq}^{mn}T_{pq}=\sum_{p=0}^{\infty}\sum_{q=1}^{\infty}T_{pq}\left\{-\int_0^{B_D}K_{xD}(z_D)\left[\int_0^1\frac{d^2\varphi_p}{dx_D^2}\frac{\varphi_m(x_D)}{\sqrt{\alpha_m\alpha_p}}dx_D\right]\frac{\Psi_q(z_D)\Psi_n(z_D)}{\sqrt{\beta_n\beta_q}}dz_D+\int_0^1\left[\int_0^{B_D}\frac{K_{zD}(z_D)}{\sqrt{\beta_n\beta_q}}\frac{d\Psi_q}{dz_D}\frac{d\Psi_n}{dz_D}dz_D\right]\frac{\varphi_p(x_D)\varphi_m(x_D)}{\sqrt{\alpha_m\alpha_p}}dx_D\right\}. \tag{B19}$$

By equating the coefficients of T_{pq}in Eq. (B19), the term F_{pq}^{mn} is expressed as:

$$F_{pq}^{mn}=-\int_0^{B_D}K_{xD}(z_D)\left[\int_0^1\frac{d^2\varphi_p}{dx_D^2}\frac{\varphi_m(x_D)}{\sqrt{\alpha_m\alpha_p}}dx_D\right]\frac{\Psi_q(z_D)\Psi_n(z_D)}{\sqrt{\beta_n\beta_q}}dz_D+\int_0^1\left[\int_0^{B_D}\frac{K_{zD}(z_D)}{\sqrt{\beta_n\beta_q}}\frac{d\Psi_q}{dz_D}\frac{d\Psi_n}{dz_D}dz_D\right]\frac{\varphi_p(x_D)\varphi_m(x_D)}{\sqrt{\alpha_m\alpha_p}}dx_D. \tag{B20}$$

Using Eq. (B1) along with the definitions of $K_{xD}(z_D)$ and $K_{zD}(z_D)$ from Eqs. (45) and (46), and partitioning the integration over individual aquifer layers, Eq. (B20) follows:

$$F_{pq}^{mn}=(M_m)^2\delta_m^p\sum_{i=1}^{3}\int_{B_{D(i-1)}}^{B_{Di}}K_{xDi}(z_D)\frac{\Psi_q(z_D)\Psi_n(z_D)}{\sqrt{\beta_n\beta_q}}dz_D+\delta_m^p\sum_{i=1}^{3}\int_{B_{D(i-1)}}^{B_{Di}}\frac{K_{zDi}(z_D)}{\sqrt{\beta_n\beta_q}}\frac{d\Psi_q}{dz_D}\frac{d\Psi_n}{dz_D}dz_D. \tag{B21}$$

Finally, substituting the explicit forms of Ψ, K_{xDi} and K_{zDi} into Eq. (B21) and evaluating the integrals yields the elements of the coefficient matrix F_{pq}^{mn} are obtained.

Last step is to establish the correspondence between the RHS terms of Eqs. (B11) and (B12). Substituting the definition of $V_i(x_D, z_D, t_D)$ from Eq. (34) into Eq. (B22), and evaluating using the property of the Dirac delta function, yields:

$$\begin{aligned}G^{mn}(t_D)&=-\frac{1}{\sqrt{\alpha_m\beta_n}}\int_0^1\int_0^{B_D}S_{sD}(z_D)\frac{\partial V}{\partial t_D}\varphi_m(x_D)\Psi_n(z_D)dx_Ddz_D-\frac{1}{\sqrt{\alpha_m\beta_n}}\int_0^1\int_0^{B_D}[\,Q_D(t_D)\delta(x_D-x_{D0})\delta(z_D-z_{D0})]\varphi_m(x_D)\Psi_n(z_D)dx_Ddz_D\\&=-\frac{1}{\sqrt{\alpha_m\beta_n}}\int_0^1\sum_{i=1}^{3}\int_{B_{D(i-1)}}^{B_{Di}}S_{sDi}(z_D)\left\{\exp\left(\frac{A_{Di}}{2}z_D\right)\sum_{k=0}^{\infty}\frac{dR_k}{dt_D}\cos(k\pi x_D)[C_{ki}\cosh(\gamma_{ki}z_D)+D_{ki}\sinh(\gamma_{ki}z_D)]\right\}\varphi_m(x_D)\Psi_n(z_D)dx_Ddz_D\\&\quad-\frac{1}{\sqrt{\alpha_m\beta_n}}Q_D(t_D)\varphi_m(x_{D0})\Psi_n(z_{D0}).\end{aligned} \tag{B22}$$

Finally, Eq. (B12) can be expressed in matrix form as:

$$\mathbf{E}\frac{d\mathbf{T}}{dt_D} + \mathbf{F}\mathbf{T}(t_D) = \mathbf{G}(t_D). \tag{B23}$$

Operating $\mathbf{E}^{-1}$ on Eq. (B23) gives:

$$\frac{d\mathbf{T}}{dt_D} + \mathbf{E}^{-1}\mathbf{F}\mathbf{T}(t_D) = \mathbf{E}^{-1}\mathbf{G}(t_D). \tag{B24}$$

The above ODE, solved over the range [0, t_D], gives (Liu el al., 2000):

$$\mathbf{T}(t_D) = \exp\left(-\mathbf{E}^{-1}\mathbf{F}t_D\right)\mathbf{T}(0) + \exp\left(-\mathbf{E}^{-1}\mathbf{F}t_D\right)\int_0^{t_D}\exp\left(\mathbf{E}^{-1}\mathbf{F}\tau\right)\mathbf{E}^{-1}\mathbf{G}(\tau)d\tau. \tag{B25}$$

The matrix exponential $\exp(-\mathbf{E}^{-1}\mathbf{F}t_D)$ in Eq. (B25) is computed using the 'expm' function in MATLAB (2025). It is important to be noted that $\mathbf{T}(0)$ represents the GITT coefficients T_{mn} at $t_D = 0$. Thus, $\mathbf{T}(0)$ is evaluated by applying the initial condition given in Eq. (37) to Eq. (B10) gives:

$$U(x_D,\ z_D,\ 0) = \sum_{m=0}^{\infty}\sum_{n=1}^{\infty} T_{mn}(0)\frac{\varphi_m(x_D)\Psi_n(z_D)}{\sqrt{\alpha_m\beta_n}} = 0 \Rightarrow T_{mn}(0) = 0. \tag{B26}$$

Finally, the coefficients $T_{mn}(t_D)$ obtained from Eq. (B25) along with Eq. (B26) are substituted into Eq. (50) to evaluate $U(x_D, z_D, t_D)$. The solution $U(x_D, z_D, t_D)$, together with $V(x_D, z_D, t_D)$, is then incorporated into Eq. (26) to obtain the dimensionless transient hydraulic head distribution in the layered regional groundwater flow basin subjected to a periodic water table boundary.

Appendix C

Table C1
Model parameter values used in the analysis.

1	Hydraulic conductivity at $z = 0$ along z direction (K_{zB_0})	1 m/d
2	Hydraulic conductivity at $z = 0$ along x direction (K_{xB_0})	10 m/d
3	Hydraulic conductivity at $z = B_1$ along z direction (K_{zB_1})	0.01 m/d
4	Hydraulic conductivity at $z = B_1$ along x direction (K_{xB_1})	0.05 m/d
5	Hydraulic conductivity at $z = B_2$ along z direction (K_{zB_2})	0.22 m/d
6	Hydraulic conductivity at $z = B_2$ along x direction (K_{xB_2})	2.23 m/d
7	Residual specific storage for the first layer (S_{sr1})	0.00001 m^{-1}
8	Residual specific storage for the second layer (S_{sr2})	0.0001 m^{-1}
9	Residual specific storage for the third layer (S_{sr3})	0.00001 m^{-1}
10	Specific storage at $z = 0$, (S_{sB_0})	0.0001 m^{-1}
11	Specific storage at $z = B_1$, (S_{sB_1})	0.001 m^{-1}
12	Specific storage at $z = B_2$, (S_{sB_2})	1.56×10^{-05} m^{-1}
13	Decay index for the top-layered aquifer (λ_1)	9.13
14	Decay index for the middle-layered aquifer (λ_2)	9.71
15	Decay index for the bottom-layered aquifer (λ_3)	9.13
16	Decay coefficient for the top-layered aquifer (A_1)	0.0025 m^{-1}
17	Decay coefficient for the middle-layered aquifer (A_2)	0.0013 m^{-1}
18	Decay coefficient for the bottom-layered aquifer (A_3)	0.0025 m^{-1}
19	Specific yield (S_y)	0.2

Data availability

Data will be made available on request.

References

Amthor, J.E., Mountjoy, E.W., Machel, H.G., 1994. Regional-scale porosity and permeability variations in Upper Devonian Leduc buildups: implications for reservoir development and prediction in carbonates. Am. Assoc. Pet. Geol. Bull. 78. https://doi.org/10.1306/A25FF215-171B-11D7-8645000102C1865D.

Aref, H., 2002. The development of chaotic advection. Phys. Fluids 14, 1315–1325. https://doi.org/10.1063/1.1458932.

Aref, H., 1984. Stirring by chaotic advection. J. Fluid. Mech. 143, 1–21. https://doi.org/10.1017/S0022112084001233.

Aryeni, T., Ginting, V., 2022. A semi-analytical solution of Richards Equation for two-layered one-dimensional soil. Adv. Water. Resour. 165. https://doi.org/10.1016/j.advwatres.2022.104199.

Azzini, I., Mara, T.A., Rosati, R., 2021. Comparison of two sets of Monte Carlo estimators of Sobol' indices. Environ. Model. Softw. 144, 105167. https://doi.org/10.1016/j.envsoft.2021.105167.

Batchelor, G.K., 1959. Small-scale variation of convected quantities like temperature in turbulent fluid Part 1. General discussion and the case of small conductivity. J. Fluid. Mech. 5, 113–133.

Bagtzoglou, A.C., Oates, P.M., 2007. Chaotic advection and enhanced groundwater remediation. J. Mater. Civ. Eng. 19, 75–83. https://doi.org/10.1061/ASCE0899-1561200719:175.

Bashist, V., Sarmah, R., Sonkar, I., 2026. Analytical solution for inverse estimation of groundwater recharge from transient thermal response in stratified media. J. Hydrol. Eng 31, 04025060. https://doi.org/10.1061/JHYEFF/HEENG-6716.

Bear, J., 1972. Dynamics of fluids in porous media. American Elsevier Publishing Company.

Brett, G.J., Pratt, L., Rypina, I., Wang, P., 2019. Competition between chaotic advection and diffusion: Stirring and mixing in a 3-D eddy model. Nonlinear. Process. Geophys. 26, 37–60. https://doi.org/10.5194/npg-26-37-2019.

Budd, D.A., 2001. Permeability loss with depth in the Cenozoic carbonate platform of west-central Florida. Am. Assoc. Pet. Geol. Bull. 85, 1253–1272. https://doi.org/10.1306/8626CAAF-173B-11D7-8645000102C1865D.

Cai, Y., Yin, Y., Kuang, X., Hao, Y., Liu, J., Zheng, C., 2023. Review: Specific storage in aquitards. Hydrogeol. J. 31, 1999–2019. https://doi.org/10.1007/s10040-023-02706-6.

Chowdhury, F., Gong, J., Rau, G.C., Timms, W.A., 2022. Multifactor analysis of specific storage estimates and implications for transient groundwater modelling. Hydrogeol. J. 30, 2183–2204. https://doi.org/10.1007/s10040-022-02535-z.

Cihan, A., Oldenburg, C.M., Birkholzer, J.T., 2022. Leakage From Coexisting Geologic Forcing and Injection-Induced Pressurization: A Semi-Analytical Solution for Multilayered Aquifers With Multiple Wells. Water. Resour. Res. 58. https://doi.org/10.1029/2022WR032343 e2022WR032343.

Cotta, R.M., 2020. Integral transforms in computational heat and fluid flow. CRC Press.

Craig, J.R., 2008. Analytical solutions for 2D topography-driven flow in stratified and syncline aquifers. Adv. Water. Resour. 31, 1066–1073. https://doi.org/10.1016/j.advwatres.2008.04.011.
Das, M., Maurya, S., Sarmah, R., 2026. Explicit representation of surface water bodies in regional groundwater flow: an analytical solution for layered heterogeneous aquifers. Model Earth Syst Env. 12. https://doi.org/10.1007/s40808-025-02626-2.
Das, M., Sarmah, R., 2025. An unsteady analytical solution for a layered Tóthian basin subjected to time-dependent water table boundary. Environ. Model. Softw. 194. https://doi.org/10.1016/j.envsoft.2025.106694.
Deng, B., Li, J., Zhang, B., Li, N., 2014. Integral transform solution for solute transport in multi-layered porous media with the implicit treatment of the interface conditions and arbitrary boundary conditions. J. Hydrol. (Amst) 517, 566–573. https://doi.org/10.1016/j.jhydrol.2014.05.072.
Efron, B., 1979. Bootstrap Methods: Another Look at the Jackknife. Ann. Stat. 7, 1–26. https://doi.org/10.1214/aos/1176344552.
Faybishenko, B., 2005. Chaotic processes in flow through fractured rock: field and laboratory experiments revisited. pp. 183–228. https://doi.org/10.1021/bk-2005-0904.ch009.
Feng, Q., Liu, Z., Zhan, H., 2021. Semi-analytical solutions for transient flow to a partially penetrated well with variable discharge in a general three-layer aquifer system. J. Hydrol. (Amst) 598, 126329. https://doi.org/10.1016/j.jhydrol.2021.126329.
Freeze, R.A., Witherspoon, P.A., 1966. Theoretical analysis of regional groundwater flow: 1. Analytical and numerical solutions to the mathematical model. Water. Resour. Res. 2, 641–656. https://doi.org/10.1029/WR002i004p00641.
Gassiat, C., Gleeson, T., Luijendijk, E., 2013. The location of old groundwater in hydrogeologic basins and layered aquifer systems. Geophys. Res. Lett. 40, 3042–3047. https://doi.org/10.1002/grl.50599.
Ghanbarian, B., Mehmani, Y., Berkowitz, B., 2023. Effect of pore-wall roughness and Péclet number on conservative solute transport in saturated porous media. Water. Resour. Res. 59. https://doi.org/10.1029/2022WR033119.
Götzfried, P., Emran, M.S., Villermaux, E., Schumacher, J., 2019. Comparison of Lagrangian and Eulerian frames of passive scalar turbulent mixing. Phys. Rev. Fluids. 4, 044607. https://doi.org/10.1103/PhysRevFluids.4.044607.
Govindaraju, R.S., Koelliker, J.K., 1994. Applicability of linearized Boussinesq equation for modeling bank storage under uncertain aquifer parameters. J. Hydrol. (Amst) 157, 349–366. https://doi.org/10.1016/0022-1694(94)90113-9.
Haberman, R., 2013. Applied partial differential equations with Fourierseries and boundary value problems, 5th ed. Pearson, London.
Hazas, M.B., Ziliotto, F., Lee, J., Rolle, M., Chiogna, G., 2023. Evolution of plume geometry, dilution and reactive mixing in porous media under highly transient flow fields at the surface water-groundwater interface. J. Contam. Hydrol. 258. https://doi.org/10.1016/j.jconhyd.2023.104243.
Hoeksema, R.J., Kitanidis, P.K., Anthony, S., 1985. Analysis of the Spatial Structure of Properties of Selected Aquifers. Water. Resour. Res. 21, 563–572.
Hong, H.S., Hickernell, F.J., Kong, H., 2003. Algorithm 823: Implementing scrambled digital sequences. ACM Trans. Math. Softw. (TOMS) 29, 95–109.
India Meteorological Department, 2022. Northeast Monsoon of South Asia. Ministry of Earth Sciences, Government of India. https://mausam.imd.gov.in/.
Jiang, X.W., Wan, L., Wang, X.S., Ge, S., Liu, J., 2009. Effect of exponential decay in hydraulic conductivity with depth on regional groundwater flow. Geophys. Res. Lett. 36, L24402. https://doi.org/10.1029/2009GL041251.
Jiang, X.W., Wang, X.S., Wan, L., 2010. Semi-empirical equations for the systematic decrease in permeability with depth in porous and fractured media. Hydrogeol. J. 18, 839–850. https://doi.org/10.1007/s10040-010-0575-3.
Jiang, X.W., Wang, X.S., Wan, L., Ge, S., 2011. An analytical study on stagnation points in nested flow systems in basins with depth-decaying hydraulic conductivity. Water. Resour. Res. 47, W01512. https://doi.org/10.1029/2010WR009346.
Kuang, X., Jiao, J.J., 2014. An integrated permeability-depth model for Earth's crust. Geophys. Res. Lett. 41, 7539–7545. https://doi.org/10.1002/2014GL061999.
Kuang, X., Zheng, C., Jiao, J.J., Cherry, J.A., Chen, J., 2021. An empirical specific storage-depth model for the Earth's crust. J. Hydrol. (Amst) 592, 125784. https://doi.org/10.1016/j.jhydrol.2020.125784.
Kumar, A., Sonkar, I., 2025. Estimability analysis and optimization of soil hydraulic and abiotic stress parameters from root zone salt-water dynamics in soil column lysimeter. Plant Soil. 513, 107–136. https://doi.org/10.1007/s11104-024-07167-8.
Lester, D.R., Metcalfe, G., Trefry, M., Dentz, M., 2025. Is chaotic advection inherent to heterogeneous Darcy flow? J. Fluid. Mech. 1018. https://doi.org/10.1017/jfm.2025.10551.
Li, Y., Zhou, Z., Zhang, N., 2024. Fractional derivative method for anomalous aquitard flow in a leaky aquifer system with depth-decaying aquitard hydraulic conductivity. Water. Res. 249. https://doi.org/10.1016/j.watres.2023.120957.
Liu, C., Szecsody, J.E., Zachara, J.M., Ball, W.P., 2000. Use of the generalized integral transform method for solving equations of solute transport in porous media. Adv. Water. Resour. 23, 483–492. https://doi.org/10.1016/S0309-1708(99)00048-2.
Liu, G., Si, B.C., 2008. Analytical modeling of one-dimensional diffusion in layered systems with position-dependent diffusion coefficients. Adv. Water. Resour. 31, 251–268. https://doi.org/10.1016/j.advwatres.2007.08.008.
MATLAB, 2025. Version R2025a. The MathWorks Inc, Natick, Massachusetts. https://www.mathworks.com.
Meunier, P., Villermaux, E., 2010. The diffusive strip method for scalar mixing in two dimensions. J. Fluid. Mech. 662, 134–172. https://doi.org/10.1017/S0022112010003162.
Mikhailov, M.D., Ozisik, M.N., 1983. Unified analysis and solutions of heat and mass diffusion. John Wiley and Sons Inc., New York, NY.
Nicholson, S.E., Dezfuli, A.K., 2013. The relationship of rainfall variability in western equatorial Africa to the tropical oceans and atmospheric circulation. Part I: The boreal spring. J Clim 26, 45–65. https://doi.org/10.1175/JCLI-D-11-00653.1.
Nicholson, S.E., Funk, C., Fink, A.H., 2018. Rainfall over the African continent from the 19th through the 21st century. Glob. Planet. Change 165, 114–127. https://doi.org/10.1016/j.gloplacha.2017.12.014.
Ottino, J.M., 1989. The kinematics of mixing: stretching, chaos, and transport. Cambridge university press.
Piskunov, N., 1969. Differential and integral calculus. Mir Publishers.
Rushton, K.R., Chan, Y.K., 1976. Pumping test analysis when parameters vary with depth. Groundwater 14, 82–87. https://doi.org/10.1111/j.1745-6584.1976.tb03637.x.
Saar, M.O., Manga, M., 2004. Depth dependence of permeability in the Oregon Cascades inferred from hydrogeologic, thermal, seismic, and magmatic modeling constraints. J. Geophys. Res. Solid. Earth. 109. https://doi.org/10.1029/2003JB002855.
Saltelli, A., Annoni, P., Azzini, I., Campolongo, F., Ratto, M., Tarantola, S., 2010. Variance based sensitivity analysis of model output. Design and estimator for the total sensitivity index. Comput. Phys. Commun. 181, 259–270. https://doi.org/10.1016/j.cpc.2009.09.018.
Sarmah, R., Sonkar, I., Chavan, S.R., 2022. Analytical solutions for predicting seepage in a layered ditch drainage system under Dirichlet and lagging Robin boundary conditions. Hydrol. Sci. J. 67, 1917–1940. https://doi.org/10.1080/02626667.2022.2101891.
Sedghi, M.M., Samani, N., Barry, D.A., 2018. Semi-analytical solution of flow to a well in an unconfined-fractured aquifer system separated by an aquitard. J. Hydrol. (Amst) 559, 895–908. https://doi.org/10.1016/j.jhydrol.2018.03.012.
Selim, H.M., 1975. Water flow through a multilayer stratified hillside. Water. Resour. Res. 11, 949–957. https://doi.org/10.1029/WR011i006p00949.
Selim, H.M., Sami Selim, M., Kirkham, D., 1975. Mathematical analysis of steady saturated flow through a multilayered soil with a sloping surface. Soil. Sci. Soc. Am. J. 39, 445–453. https://doi.org/10.2136/sssaj1975.03615995003900030024x.
Shestakov, V.M., 2002. Development of relationship between specific storage and depth of sandy and clay formations. Environ. Geol. 42, 127–129. https://doi.org/10.1007/s00254-001-0481-z.
Souvik, C., Maity, P.K., Das, S., 2020. Investigation, simulation, identification and prediction of groundwater levels in coastal areas of Purba Midnapur, India, using MODFLOW. Env. Dev Sustain 22, 3805–3837. https://doi.org/10.1007/s10668-019-00344-1.
Sposito, G., 2006. Chaotic solute advection by unsteady groundwater flow. Water. Resour. Res. 42. https://doi.org/10.1029/2005WR004518.
Srivastava, K., Rai, S.N., Singh, R.N., 2002. Modeling water-table fluctuations in a sloping aquifer with random hydraulic conductivity. Environ. Geol. 41, 520–524. https://doi.org/10.1007/s002540100385.
Suk, H., Chen, J.S., Han, W.S., Park, E., 2022. New semi-analytical solutions to the radial advection-dispersion equation for solute transport in a transient divergent radial flow. Adv. Water. Resour. 167. https://doi.org/10.1016/j.advwatres.2022.104283.
Tajima, S., Dentz, M., 2025. Transient forcing in heterogeneous aquifers drives solute containment and chaotic mixing. Adv. Water. Resour. 203. https://doi.org/10.1016/j.advwatres.2025.105021.
Tóth, J., 1962. A theory of groundwater motion in small drainage basins in Central Alberta. Can. J Geophys Res 67, 4375–4387. https://doi.org/10.1029/JZ067i011p04375.
Tóth, J., 1963. A theoretical analysis of groundwater flow in small drainage basins. J. Geophys. Res. 68, 4795–4812. https://doi.org/10.1029/JZ068i016p04795.
Trefry, M.G., Lester, D.R., Metcalfe, G., Ord, A., Regenauer-Lieb, K., 2012. Toward enhanced subsurface intervention methods using chaotic advection. J. Contam. Hydrol. 15–29. https://doi.org/10.1016/j.jconhyd.2011.04.006.
Trefry, M.G., Lester, D.R., Metcalfe, G., Wu, J., 2019. Temporal fluctuations and poroelasticity can generate chaotic advection in natural groundwater systems. Water. Resour. Res. 55, 3347–3374. https://doi.org/10.1029/2018WR023864.
Vandenberg, A., 1980. Regional groundwater motion in response to an oscillating water table. J. Hydrol. (Amst) 47, 333–348. https://doi.org/10.1016/0022-1694(80)90102-X.
Wang, J.Z., Jiang, X.W., Wan, L., Wörman, A., Wang, H., Wang, X.S., Li, H., 2015. An analytical study on artesian flow conditions in unconfined-aquifer drainage basins. Water. Resour. Res. 51, 8658–8667. https://doi.org/10.1002/2015WR017104.
Wang, J.Z., Jiang, X.W., Zhang, Z.Y., Wan, L., Wang, X.S., Li, H., 2017. An analytical study on three-dimensional versus two-dimensional water table-induced flow patterns in a Tóthian basin. Hydrol. Process. 31, 4006–4018. https://doi.org/10.1002/hyp.11317.
Wang, X.S., Jiang, X.W., Wan, L., Song, G., Xia, Q., 2009. Evaluation of depth-dependent porosity and bulk modulus of a shear using permeability-depth trends. Int. J. Rock Mech. Min. Sci. 46, 1175–1181. https://doi.org/10.1016/j.ijrmms.2009.02.002.
Wang, X.S., Wan, L., Jiang, X.W., Li, H., Zhou, Y., Wang, J., Ji, X., 2017. Identifying three-dimensional nested groundwater flow systems in a Tóthian basin. Adv. Water. Resour. 108, 139–156. https://doi.org/10.1016/j.advwatres.2017.07.016.
Zhang, P., DeVries, S.L., Dathe, A., Bagtzoglou, A.C., 2009. Enhanced mixing and plume containment in porous media under time-dependent oscillatory flow. Env. Sci Technol 43, 6283–6288. https://doi.org/10.1021/es900854r.
Zhang, J., Liang, X., Zhang, Y., Chen, X., Ma, E., Schilling, K., 2022. Groundwater responses to recharge and flood in riparian zones of layered aquifers: An analytical model. J. Hydrol. (Amst) 614, 128547. https://doi.org/10.1016/j.jhydrol.2022.128547.
Zhang, Z.Y., Jiang, X.W., Zhou, P.Y., Batelaan, O., Wang, X.S., Han, P.F., Wan, L., 2025. Stagnation and pseudo-stagnation lines for separating 3D groundwater flow systems in Tóthian basins. Water. Resour. Res. 61. https://doi.org/10.1029/2024WR038967.

Zhao, K.Y., Jiang, X.W., Wang, X.S., Wan, L., Wang, J.Z., Wang, H., Li, H., 2018. An analytical study on nested flow systems in a Tóthian basin with a periodically changing water table. J. Hydrol. (Amst) 556, 813–823. https://doi.org/10.1016/j.jhydrol.2016.09.051.

Zhao, Z., Illman, W.A., 2021. On the importance of considering specific storage heterogeneity in hydraulic tomography: Laboratory sandbox and synthetic studies. J. Hydrol. (Amst) 593. https://doi.org/10.1016/j.jhydrol.2020.125874.

Zhuang, C., Yan, L., Kuang, X., Zhan, H., Illman, W.A., Dou, Z., Zhou, Z., Wang, J., 2024. Statistical characteristics of aquitard hydraulic conductivity, specific storage and porosity. J. Hydrol. (Amst) 643. https://doi.org/10.1016/j.jhydrol.2024.132066.

Zlotnik, V.A., Cardenas, M.B., Toundykov, D., 2011. Effects of multiscale anisotropy on basin and hyporheic groundwater flow. Groundwater 49, 576–583. https://doi.org/10.1111/j.1745-6584.2010.00775.x.

Zlotnik, V.A., Toundykov, D., Cardenas, M.B., 2015. An analytical approach for flow analysis in aquifers with spatially varying top boundary. Groundwater 53, 335–341. https://doi.org/10.1111/gwat.12205.